

A Bioinspired Plasmonic Nanocomposite Actuator Sunlight-Driven by a Photothermal-Hygroscopic Effect for Sustainable Soft Robotics

Stefano Mariani,* Luca Cecchini, Alessio Mondini, Emanuela Del Dottore, Marilena Ronzan, Carlo Filippeschi, Nicola Maria Pugno, Edoardo Sinibaldi,* and Barbara Mazzolai*

Combined photothermal-hygroscopic effects enable novel materials actuation strategies based on renewable and sustainable energy sources such as sunlight. Plasmonic nanoparticles have gained considerable interest as photothermal agents, however, the employment in sunlight-driven photothermal-hygroscopic actuators is still bounded, mainly due to the limited absorbance once integrated into nanocomposite actuators and the restricted plasmonic peaks amplitude (compared to the solar spectrum). Herein, the design and fabrication of an AgNPs-based plasmonic photothermal-hygroscopic actuator integrated with printed cellulose tracks are reported (bioinspired to Geraniaceae seeds structures). The nanocomposite is actuated by sunlight power density (i.e., 1 Sun = 100 mW cm⁻²). The plasmonic AgNPs are in situ synthesized on the PDMS surface through a one-step and efficient fluoride-assisted synthesis (surface coverage ≈40%). The nanocomposite has a broadband absorbance in the VIS range (>1) and a Photothermal Conversion Efficiency ≈40%. The actuator is designed exploiting a mechanical model that predicted the curvature and forces, featuring a $\approx 6.8 \pm 0.3$ s response time, associated with a ≈43% change in curvature and a 0.76 ± 0.02 mN force under 1 Sun irradiation. The plasmonic nanocomposite actuator can be used for multiple tasks, as hinted through illustrative soft robotics demonstrators, thus fostering a bioinspired approach to developing embodied energy systems driven by sunlight.

1. Introduction

Soft material systems, and in particular soft robots, actuated by environmental energy sources offer great potential for developing sustainable robotics and environmental applications.^[1–4]


In this regard, Nature offers priceless sources of inspiration, including many plants and seeds that adaptively leverage environmental stimuli, including humidity and sunlight, to effectively move and interact with their ecosystems.^[5–9]

For example, pinecones,^[5,6] wheat,^[7] and Geraniaceae seed structures^[8] adsorb water molecules (from environmental moisture) onto locally-aligned hygroscopic cellulose-based microstructures in the cells, thus enacting shape changes functional to lifecycle tasks (e.g., opening/close in pinecones^[5,6] and locomotion in wheat and Geraniaceae seeds),^[7,8] aimed at seeds dispersal and germination.

Complementarily, juvenile sunflower plants track the Sun's movement thanks to the circadian rhythms that regulate

S. Mariani, L. Cecchini, A. Mondini, E. Del Dottore, M. Ronzan, C. Filippeschi, E. Sinibaldi, B. Mazzolai
Bioinspired Soft Robotics Laboratory
Istituto Italiano di Tecnologia
Via Morego 30, Genova 16163, Italy
E-mail: stefano.mariani@iit.it; edoardo.sinibaldi@iit.it;
barbara.mazzolai@iit.it

L. Cecchini, N. M. Pugno
Laboratory for Bioinspired
Bionic
Nano
Meta Materials and Mechanics
Department of Civil
Environmental and Mechanical Engineering
University di Trento
Via Mesiano 77, Trento 38123, Italy
N. M. Pugno
School of Engineering and Materials Science
Queen Mary University of London
Mile End Road, London E1 4NS, United Kingdom

 The ORCID identification number(s) for the author(s) of this article can be found under <https://doi.org/10.1002/admt.202202166>

© 2023 The Authors. Advanced Materials Technologies published by Wiley-VCH GmbH. This is an open access article under the terms of the Creative Commons Attribution License, which permits use, distribution and reproduction in any medium, provided the original work is properly cited.

DOI: 10.1002/admt.202202166

the east-west asymmetric elongation of cells modulated by the auxin signaling pathway, thereby enhancing plant growth and pollinator visits to the flowers.^[9]

Overall, Plants and seeds offer a wide range of actuation mechanisms with energy consumption powered by environmental stimuli.

For this reason, artificial actuation systems inspired by plants have been proposed, with growing interest, in stimuli-responsive material through hygroscopic actuation. In this regard, moisture-responsive multilayers, capable of bending upon exposure to humidity, based on the differential geometric, mechanical, and hygroscopic properties of the involved layers, have been investigated.^[10–15]

Differently, light-responsive actuators have been mostly studied by focusing on specific material properties as well as *trans–cis* isomerization (e.g., in azobenzene-based molecules)^[16] or photothermal conversion^[17,18] (e.g., in MXenes,^[19–22] Graphene,^[23–25] Carbon Nanotubes (CNTs)^[26] and Metal Nanoparticles (MNPs).^[27–32]

In general, once photoexcitation converts into heat, multiple transduction pathways can be implemented to achieve actuation, e.g., through thermal expansion/contraction, water adsorption/desorption, phase change, and modulation of the physicochemical properties of the involved (nano) composites, and additional effects such as, e.g., the creation of surface tension gradients.^[18] Finally, some efforts have been devoted to the use of photothermal conversion to induce reversible water adsorption/desorption, thus coupling photothermal and hygroscopic approaches to achieve reversible actuation.^[18–21,24,25]

However, photothermal-humidity driven actuation in multilayered structures based on non-coherent and low-power-density light sources, as provided by ordinary solar radiation (e.g., UV–Vis radiation with a power density of 1 Sun = 100 mW cm^{−2}), is highly requested to exploit such a ubiquitously available natural power source. This could effectively open new avenues for sustainable actuation strategies, but it still poses a tremendous challenge.

Examples of photothermal-hygroscopic driven actuation at power densities comparable to solar radiation rely on the integration of high Photothermal Conversion Efficiency (P.C.E.) materials based on Carbon (e.g., CNT and graphene)^[18] (P.C.E. ≈ 80%–90%) and MXene (P.C.E. ≈ 100%).^[20,33]

Despite the high P.C.E., integration of these materials into sunlight-driven actuators introduces several issues. For instance, MXene requires long (48 h) synthesis and elaborated purification and functionalization steps.^[19,20] Moreover, MXene, graphene, and CNTs are usually *ex-situ* integrated^[19,20] in the nanocomposites.

Alternatively, thermoplasmonic metal nanoparticles (MNPs) with localized surface plasmon resonances (LSPR) have gained considerable interest due to their ability to manipulate light from solar energy at the nanometer scale and convert it into heat for energetically sustainable development purposes.^[34] However, the applications in photothermal-hygroscopic actuators, driven by only sunlight, are still to be demonstrated due to the relatively restricted LSPR peaks amplitude (compared to the solar spectrum amplitude) and the poor functionalization yield in nanocomposite materials.

Here we report the first fully NPs-based plasmonic and photothermal-hygroscopic actuator driven by sunlight. Specifically, a trilayer structure was implemented, with a PDMS base layer (BL) for structural support upon that a nanometric middle AgNPs layer (Plasmonic Photothermal Layer, PPTL) was synthesized for exploiting heat generation upon solar radiance, and an upper anisotropically hygroscopic layer (HL), based on cellulose, devised to finally transduce actuation through bending.

As regards the photothermal mechanism, the AgNPs were synthesized by adapting a single-step, *in situ*, and fluoride-assisted synthesis reduction protocol recently disclosed by Mariani et al.,^[35,36] only using the PDMS layer (as reducing agent) and AgF in ethanolic solution. Such a novel synthesis allowed the achievement of high-yield surface coverage (40%) of AgNPs firmly anchored to the PDMS surface, with broadband and high absorption value in the visible range (>1) and a P.C.E. ≈ 40% under 1 Sun irradiation (100 mW cm^{−2}).

As regards the hygroscopic mechanism, aligned tracks of hygroscopic carboxymethyl cellulose (CMC) were printed on the BL/PPTL actuator by taking inspiration from the Geraniaceae seed structure of *Pelargonium appendiculatum* (L.fil.) Willd. Since cellulose materials have a hygroscopic and water-swelling nature thanks to the abundant hydrophilic groups, we adopted CMC because it is an anionic charged cellulose derivative with a more pronounced water-swelling ratio than native cellulose.^[37]

Thanks to the photothermal effect of AgNPs, the loss of humidity induced in the CMC enacts actuation, with strong curvature changes (over 40%) in a short response time (6.8 ± 0.3 s) and a force generation of 0.76 ± 0.02 mN under 1 Sun irradiation.

A purposely theoretical model predicted the kinematics and the statics under controlled humidity exposure.^[38]

Moreover, crawling, coiling/rolling, gripping, and weightlifting capabilities were also demonstrated for a rectangular actuator, as well as shape reconfiguration illustrated by implementing the trilayer into an actuator devised for programmed motion responsive to sunlight.

The achieved results disclose the possibility of using sunlight to drive photothermal-hygroscopic actuators based only on plasmonic MNPs as photothermal agents. Besides avoiding the criticalities associated with actuator implementations based on MXene, graphene, and CNT, while also matching the related performance in terms of light power densities vs response times (few seconds) (Figure S1, Supporting Information), the obtained results pave the way for a novel class of hygroscopic soft actuators driven by natural environmental conditions, thus fostering the energetically sustainable development of soft material, actuators, and robots.

2. Results and Discussions

Figure 1a and Figure S2 (Supporting Information) illustrate the fabrication of the plasmonic photothermal-hygroscopic nanocomposites consisting in: 1) PDMS preparation (Base Layer, BL); 2) *in situ* synthesis of plasmonic AgNPs exploiting a recent and high yield fluoride-assisted techniques developed by Mariani et al.,^[35,36] (Plasmonic Photothermal Layer, PPTL); CMC printing using Direct Ink Writing (Video S1, Supporting Information) (Hygroscopic Layer, HL). The multilayered structure

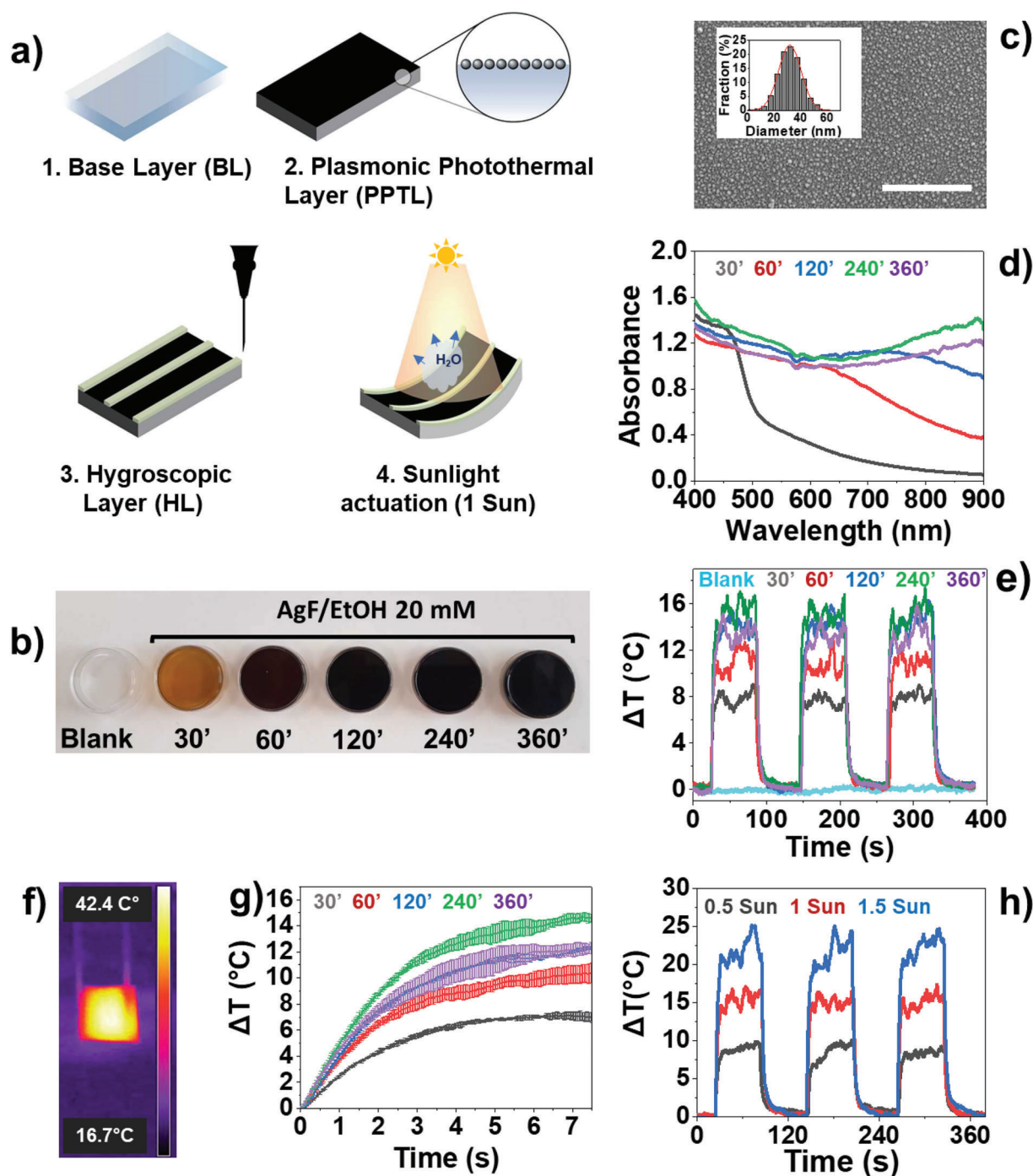


Figure 1. a) Fabrication sketch of the photothermal-hygroscopic actuator consisting of: 1. PDMS preparation (Base Layer, BL); 2. In situ synthesis of plasmonic AgNPs through a fluoride-assisted method (Plasmonic Photothermal Layer, PPTL); 3. Carboxymethyl Cellulose (CMC) printing on PPTL through Direct Ink Writing (DIW) (Hygroscopic Layer, HL); 4. Photothermal-hygroscopic actuation under 1 Sun. b) Pictures of PDMS prepared in Petri dishes and decorated with AgNPs in a fluoride solution (i.e., 20 mM AgF) for 30–360 min. c) SEM image of the PDMS surface decorated with AgNPs for 240 min. Scalebar is 1 μm . In the inset is reported the AgNPs distribution. d) Absorbance spectra of PDMS decorated with AgNPs reported in (b). e) Temperature variations ($\Delta T, ^\circ\text{C}$) over time on the PDMS/AgNPs samples reported in (b) and exposed to a solar simulator light with a power density of 100 mW cm^{-2} with intermitting solar irradiation (60 s irradiation/60 s of darkness). f) Photothermal camera image of the PDMS surface decorated with AgNPs for 240 min and exposed to a solar simulator light with a power density of 100 mW cm^{-2} . The thermal color scale shows the maximum and minimum temperature values recorded in the image. g) Synchronized temperature variations ($\Delta T, ^\circ\text{C}$) over time on the PDMS/AgNPs samples reported in (b) and exposed to a solar simulator light with a power density of 100 mW cm^{-2} . Data are provided as average values over 3 replicates with error bars representing one standard deviation. h) Temperature variations ($\Delta T, ^\circ\text{C}$) over time on the PDMS sample with AgNPs decorated for 240 min and exposed to solar simulator light with different power densities of 50, 100, and 150 mW cm^{-2} (0.5, 1, and 1.5 Sun) and with intermitting solar irradiation (60 s irradiation/60 s) of darkness.

BL/PPTL/HL was actuated by photothermal-hygroscopic effect under 1 Sun irradiation.

The thickness of the PDMS (BL) was $49 \pm 4 \mu\text{m}$ (N samples = 8) (Figure S3, Supporting Information). AgNPs were formed on the PDMS adapting the one-step and in situ redox reaction occurring between unreacted Si–H bonds of the curing agent and Ag^+ available in the ethanolic AgF solution. The fluoride ions in the metal solution improved density and accelerated the kinetics of the synthetic process with respect to state-of-the-art fluoride-free approaches.^[35]

Figure 1b shows both blank PDMS (not decorated, BL) and PDMS decorated with AgNPs by casting 20 mM AgF ethanolic solutions for different times (PPTL), namely from 30 to 360 min. PDMS showed from brownish to black color intensities increasing with the decoration time.

This effect is ascribable to Localized Surface Plasmon Resonance (LSPR) cumulative absorption of the formed NPs, which increase both in size^[39] and distribution, combined with a plasmonic interparticle coupling as previously reported both for AgNPs (adsorbed onto solid surfaces)^[40] and AuNPs in liquid solutions.^[41]

SEM analysis of the PDMS petri decorated in ethanolic solutions of AgF at 60, 120, 240, and 360 min is reported in Figure 1c and Figure S4 (Supporting Information). SEM EDX analysis reported in Figure S5 (Supporting Information), for the AgNPs synthesis of 240 min, shows the appearance of a strong Ag signal (Weight% = $63.88 \pm 0.35\%$) due to the in situ synthesis. It is interesting to note that the oxygen signal (due to Si–O–Si bonding in the PDMS structure) is higher (Weight% = $11.26 \pm 0.58\%$) compared to the expected one (Weight% = 9.28%) and this is due to the oxidation of the silicon during the in situ redox reaction as reported in^[42,43].

The AgNPs average sizes increased from 21 to 35 nm as the decoration time increased from 60 to 360 min. All the NPs distributions were well fitted by Gaussian profiles ($R^2 = 0.99$) (Figure S6a–e, Supporting Information).

The surface coverage of the AgNPs was 23.31%, 40.36%, 40.72%, and 41.02%, for 60, 120, 240, and 360 min of decoration, respectively Figure S6f (Supporting Information).

We monitored the decoration process by using absorption spectroscopy (Figure 1d) after the measurement of the reflectance and transmittance spectra in the visible range (400–900/1000 nm) (Figure S7a–c, Supporting Information) given that the sunlight simulator has significant irradiance values only between 400–1000 nm (Figure S8, Supporting Information). In the spectrum recorded at $t = 30$ min an intense absorption peak ($A_{\text{max}} \sim 1.4$) appeared at 400 nm, which was associated with the LSPR of the spherical AgNPs.^[35] At $t = 60$ and 120 min the LSPR had a broader band, which agreed with: the increase in AgNPs size; the broadening of the distribution recorded (Figure S6, Supporting Information); the increase of the surface coverage (Figure S6f, Supporting Information) and the interparticle coupling.^[40] At $t = 240$ and 360 min, a further broadening of the LSPR peaks was observed with an absorbance value over the whole wavelength range (400–900 nm) of roughly 1.2 and 1.1. The higher absorbance value for the sample synthesized after 240 min compared to the 360 min could be explained by the lower reflectance (Figure S7c, Supporting Information).

The synthesized BL/PPTL nanocomposites were then tested in photothermal conversion upon irradiation with visible light by simulating the sunlight radiation, with a power density of 100 mW cm^{-2} (1 Sun) in air and using a thermocamera (Figure 1e–g).

All the photothermal profiles showed an increase in temperature over time well-fitted with an asymptotic exponential trend ($R^2 = 0.99$) as reported in Figure S9a–e (Supporting Information). The trend of the maximum ΔT ($^{\circ}\text{C}$) vs decoration times reached the maximum value in the BL/PPTL samples decorated for 240 min with AgNPs ($\Delta T \sim 14.6 \pm 0.3 \text{ }^{\circ}\text{C}$ after 7 s of irradiation, N samples = 3). This decoration also showed the highest temperature gradient upon illumination (Figure S9f, Supporting Information) ($7.3 \pm 0.4 \text{ }^{\circ}\text{C/s}$ for $t = 0$ s, N samples = 3).

For completeness, the photothermal properties of such BL/PPTL layer were also evaluated at other sunlight power densities (i.e., 0.5 and 1.5 Sun) (Figure 1h; Figure S10, Supporting Information) and under IR laser irradiation at 808 nm at high power density (1586 mW cm^{-2}) (Figure S11, Supporting Information). Under laser irradiation, the surface temperature reached the value of $208.2 \pm 0.6 \text{ }^{\circ}\text{C}$ (N sample = 3) in 7 s. Interestingly the reached value was higher than the one obtained using a PDMS layer with a similar thickness ($66 \mu\text{m}$) and covered with graphene (one of the most exploited materials for photothermal actuation) and AuNPs as photothermal enhancers i.e., $\approx 150 \text{ }^{\circ}\text{C}$ under an IR laser (808 nm) and a similar irradiation power (3000 mW cm^{-2}).^[24]

The photothermal conversion efficiency (PCE, η) was calculated by adapting the methods used in liquid-NPs solutions^[44] to thin films suspended in air (Section S3, Supporting Information).

The PCE results for single wavelength laser source and broad solar spectrum agreed: 41.7% and 40.8%, respectively.

We tested the adhesion properties of AgNPs formed on PDMS in a 20 mM AgF ethanolic solution for 240 min (Figure S12, Supporting Information). The reflectance spectra recorded before and after the adhesion test were identical confirming the high adhesion between the PDMS and AgNPs.

Differently from the conventional premixing of photothermal agents (e.g., CNT),^[45] the in situ synthesis of AgNPs onto the PDMS surface did not change significantly mechanical properties. Young's Modulus of PDMS and PDMS/AgNPs (240 min synthesis) were not statistically different being $2.55 \pm 0.52 \text{ MPa}$ and $1.95 \pm 0.34 \text{ MPa}$, respectively.

For the above-mentioned reason, the BL/PPTL sample decorated for 240 min with AgNPs was used for the subsequent development of the photothermal-hygroscopic actuator.

We designed the BL/PPTL/HL actuator (Figure 2a), taking inspiration from the morphometric structure of the Geraniaceae seeds (i.e., *Pelargonium appendiculatum*) (Figure 2b–d). These seeds are characterized by a central body, the awn, which shows hygroscopic actuation to promote spreading, soil penetration, and germination. As shown in the section view of the awn (Figure 2c,d), the structure can be decomposed as an effective bilayer, with an oriented and parallel cellulose distribution, as hygroscopic layer, and a lignin-based layer.^[7]

To guarantee adhesion between hydrophobic PDMS/AgNPs substrate and hydrophilic cellulose layer, we used air plasma

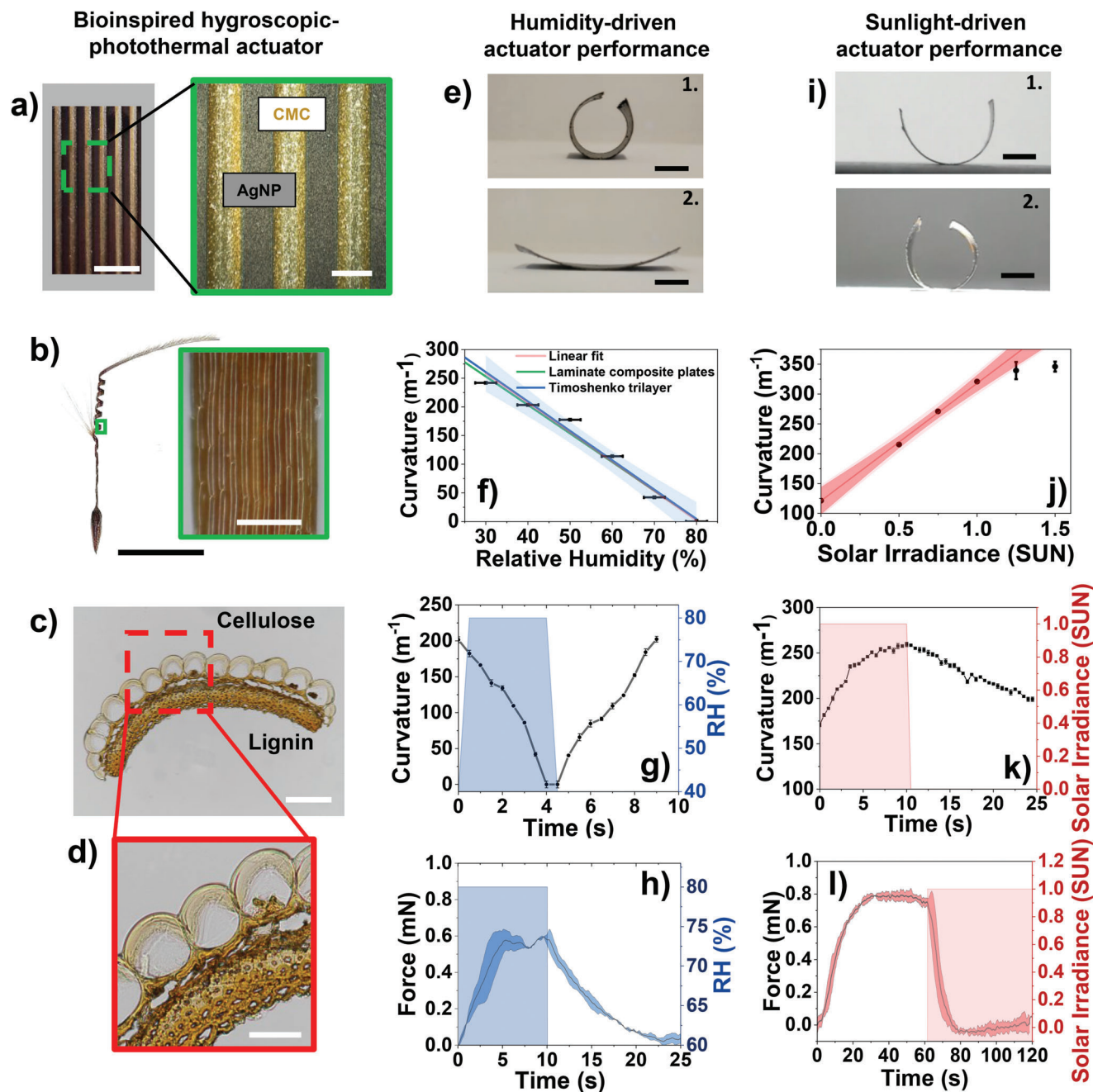


Figure 2. a) Picture of the BL/PPTL/HL actuator showing the AgNPs region (brown, BL/PPTL) and printed, aligned, and parallel CMC tracks (yellow tracks, HL). Scale bar is 0.5 cm. The inset shows a zoom from (a). Scale bar is 1 mm. b) Picture of a *Pelargonium appendiculatum* seed. Scale bar is 1 cm. The inset shows the microfibrils cellulose structure. Scalebar is 200 μm . c) White image of a transversal section of the awn in the cellulose- and lignin-based regions. Scalebar is 100 μm . d) Zoom from (c) showing the cellulose-based region. Scale bar is 50 μm . e) Pictures of the BL/PPTL/HL actuator exposed to relative humidity (%RH) equal to 30% (1) and 80% (2). f) Curvature of the actuator vs relative humidity (30%–80%). Data are fitted by linear regression and in good agreement with the laminate composite plates model and the Timoshenko trilayer model. g) Curvature of the actuator vs time (s) with %RH changing from 40% to 80% (average %RSD = 2.7%, N sample = 3). h) Forces (mN) vs time (s) with %RH changing from 40% to 80%. i) Pictures of the actuator exposed to 0 Sun (1) and 1 Sun (2) at a fixed %RH = 60%. j) Curvature variation of the actuator vs time (s) exposed to 0–1.5 Sun at a fixed %RH = 60%. k) Curvature variation of the actuator vs time (s) exposed to 1 Sun (average %RSD = 0.7%, N sample = 3). l) Force (mN) vs time (s) of the actuator exposed to 1 Sun at a fixed %RH = 60%. In f–h and j–l data are provided as average values over 3 replicates with error bars representing one standard deviation.

followed by the nanometric coating with PVA, as described in the protocol reported in.^[46] The combined plasma oxidation and PVA treatment have been reported to be long-term stable, ensuring long-term hydrophilicity of the PDMS surfaces in contrast to the only plasma oxidized PDMS, which tends to regain its surface hydrophobicity 1 day after treatment. The increase in hydrophilicity was confirmed by the contact angle analysis reported in Figure S13 (Supporting Information). Figure S14 (Supporting Information) shows the thickness of the PVA coating (≈ 60 nm) on the blank PDMS layer. Such values agree with those reported in the literature for similar spin coating protocols.^[47]

SEM EDX analysis reported in Figure S5 (Supporting Information), for the AgNPs synthesis of 240 min before and after the use of air plasma shows the O% weight increases from $11.26 \pm 0.58\%$ to $11.87 \pm 0.10\%$ ($N = 3$). However, this increase could not be considered statistically significant (Student's t-test confidence level = 95%). Also, the temperature variations ($\Delta T, ^\circ\text{C}$) over time (s) under sunlight exposure (1 Sun) did not show a significant variation of the photothermal properties due to the air plasma (Figure S15, Supporting Information).

Based on the mechanical characterization of the materials, PDMS/AgNPs and CMC (Figure S16, Supporting Information), we designed the CMC layer (considering an equivalent thickness, obtained by averaging the CMC tracks thickness and the inter-track distances) to predict the curvature and so, to properly design the actuator (Figures S17–S19, Supporting Information). To this purpose, we considered both Timoshenko beam model, and the laminate composite plates model (Section S4, Supporting Information).^[38] In particular, we consider the actuator as a tri-layered structure, in which the PDMS/AgNPs passive substrate is stacked with a PVA buffer layer, and the hygroscopic CMC layer is deposited on the topmost part.

CMC hydrogel (10% in deionized water) was printed via DIW (Video S1, Supporting Information) on the activated PDMS/AgNPs surface and totally dried in the oven to obtain a pattern of CMC tracks wide 0.91 ± 0.06 mm (N samples = 6), distanced 0.67 ± 0.02 mm (N samples = 6) (Figure 2a; Figure S20, Supporting Information) and thick 20.8 ± 2.1 μm (N samples = 6) (Figure S21, Supporting Information). Accordingly, with the Section S4 (Supporting Information), an equivalent thickness equal to 13.5 ± 2.5 μm was calculated.

We tested the adhesion properties of CMC on PDMS/AgNPs surface (Figure S22, Supporting Information). The surficial microscopy images captured after the adhesion test proved the integrity of the CMC tracks and the good adhesion between the PDMS/AgNPs and CMC mediated by PVA (Figure S22, Supporting Information).

Considering the key role played by hygroscopic actuation in the proposed multi-physics-driven system, we preliminarily characterized the actuator response versus RH only.

We first addressed the hygromorphic behavior of the considered actuator regarding both its kinematics (curvature) and statics (force) performance as a function of %RH. When the environmental %RH decreased, it induced a contraction of the CMC tracks, thus increasing actuator curvature (positive curvature intended as the folding of the hygroscopic layer) (Figure 2e.1); reciprocally, a decrease in %RH caused a reduction in the actuator curvature, i.e., to unbend (Figure 2e.2), as reported in Video S2 (Supporting Information).

Considering that, at least at a first approximation, the curvature of a thin multilayer (plate) can be modeled regardless of sample width (w) and length (l),^[48] so that actuation force is consequently computed per unit width,^[10] we fixed the geometrical dimensions of the rectangular sample actuator as $w = 1$ cm and $l = 2$ cm.

We characterized the curvature response in a climatic chamber (Figure 2f). From the recorded data, we also extracted the humidity value $\Phi_0 = 80\%$ associated with null curvature, to be used for model calibration (Section S4, Supporting Information). Both laminate composite plates and Timoshenko model predicted the curvature response within 95% confidence interval. These results highlighted that we can accurately control the actuator curvature based on RH.

We then proceeded to analyze the time response of the hygroscopic actuator. Considering that water adsorption in the cellulose layer was driven by diffusion,^[10,15] we first characterized the time evolution of the curvature by increasing the humidity level (step increase from 40% to 80%) using deionized water aerosol (i.e., working conditions over the diffusion limit).

Figure 2g shows the time behavior of the actuator subjected to an RH stepwise function. During water adsorption, the structure decreased its curvature from $\kappa = 2.01 \pm 0.15$ to $\kappa = 0 \pm 0.12$ cm^{-1} in $\tau_{\text{RH}} = 4.11 \pm 0.23$. Moreover, considering that the actuation was mediated by Fickian diffusion upon the cellulose layer, the diffusivity of the CMC layer could be evaluated as $D_{\text{CMC}} \approx h_{\text{CMC}}^2 / \tau_{\text{RH}} = 2.94 \pm 0.34 \times 10^{-11}$ m^2s^{-1} .

Figure 2h reports the force produced by the hygroscopic actuation (under quasi-static conditions) by varying the humidity level from RH = 60% to RH = 80%, with the maximum force equal to $F_{\text{RH}} = 0.57 \pm 0.07$ mN. The considered force was predicted by both the Timoshenko model ($F_{\text{T}} = 0.58$ mN) and the laminate composite plates model ($F_{\text{LC}} = 0.56$ mN) within a confidence interval of 95% (Figures S23 and S24, Supporting Information). The force estimate turned out to be in good agreement with the experimental results (thus corroborating the working assumptions introduced for ease of model derivation (Section S4, Supporting Information, Equations S7 and S8).

Thanks to the photothermal effect, we promoted water desorption by increasing the substrate temperature with a broad solar spectrum with 1 Sun power density. Considering water adsorption enthalpy, an increase in temperature at constant environmental RH led to a bending of the actuator (Figure 2i and Video S2, Supporting Information). An increase in temperature determined an increase in the rate of humidity desorption and so, the localized amount of humidity in the cellulose layer was consequently reduced.

At first approximation, the solar irradiance and humidity could be analyzed as independent variables. We characterized the kinematics and statics of the actuator by varying the optical power density (0.5–1.5 Sun) at a fixed initial (RH = 60%) humidity level (Figure 2j). The curvature shows a linear trend ($R^2 = 0.99$) up to 1 Sun of solar irradiance, above that curvature saturation occurs. Based on the previous characterization results on purely hygroscopic actuation, the residual RH was < 20% on the cellulose layer for solar irradiance > 1 Sun.

Figure 2k shows the response of the load-free actuator driven at 1 Sun (step application of the solar irradiance). Here, we can observe the combined effect of photothermal conversion and water desorption. The actuator changed its curvature from $\kappa = 1.71 \pm 0.05$ to $\kappa = 2.54 \pm 0.03$ cm^{-1} in $t_{\text{Sun}} = 6.8 \pm 0.3$ s.

Figure S25 (Supporting Information) illustrates actuation performance retention over 100 cycles of irradiation: bending curvature changed by only 5% in not irradiation conditions and roughly 0.5% under 1 Sun irradiation, respectively.

In Figure 2l we finally analyzed the static performance when the actuator was irradiated with a stepwise function from 0 to 1 Sun, reaching a maximum force of $F_{\text{Sun}} = 0.76 \pm 0.02$ mN. Interestingly, the corresponding force (≈ 1 mN) was associated to a moment ($\approx 10^{-5}$ N m) in the same order of magnitude to those of Geraniaceae seeds (e.g., *Pelargonium appendiculatum* and *Erodium malacoides*), as reported in Figure S26 (Supporting Information).

To illustrate the potential for application of the proposed BL/PPTL/HL actuator, while keeping implementation efforts in line with the present developmental stage, we introduced several sunlight-driven demonstrators, namely grasper, crawler, coiler/roller, weightlifter, and a final reconfiguration obtained by implementing an actuator devised for uniaxial programmed motion responsive to sunlight (Figure 3).

The BL/PPTL/HL actuator (2 cm \times 1 cm \times 0.006 cm, mass 13.9 ± 0.9 mg, N samples = 6) could act as a wireless soft grasper (Figure S27a, Supporting Information). The soft grasper is shown in Figure 3a and Video S3 (Supporting Information). With light exposure (1 Sun), the bilayer bent to grip a cargo with size (14 cm \times 1.70 cm \times 0.75 cm, mass 156 mg). When the light was turned off the cargo was released. In the reported test, the grasper handled a cargo with a mass greater than 11-fold its mass (and a volume greater than ≈ 1500 -fold its volume).

A crawler demonstrator (with the same embodiment of the previous grasper) is shown in Figure 3b and Video S4 (Supporting Information). Locomotion was driven by cyclic irradiance, leading to cyclic contraction/extension of the crawler structure (it contracted under sunlight actuation, and stretched back upon irradiation removal). A constant unidirectional movement was obtained thanks to the different friction forces between the two ends of the actuator, modified with 5 iron threads in front (bent at 110°) and 5 behind (straight), respectively. The proposed crawler moves at ≈ 1 BL min^{-1} considering the experimental variation of irradiance as function of time. Considering the driving illumination, the crawler moves at 0.3 BL Sun^{-1} cycle.

Lifting tests on such demonstrators were also reported using payloads of 42.6 and 144.1 mg (≈ 3 and 10-fold the actuator mass) (Video S5, Supporting Information). Under sunlight exposure, the actuator could lift the 42.6 mg payload of 4 mm (work ≈ 1.7 μJ) and the 144.1 mg payload of 2 mm (work ≈ 2.8 μJ), corresponding to an energy density of 0.14 and 0.23 kJ m^{-3} , respectively.

A demonstrator capable of coiling/uncoiling (4.5 cm \times 0.5 cm \times 0.006 cm) (Figure 3d) was also implemented (Video S6, Supporting Information), by laying the CMC tracks at a 20° angle with respect to the actuator longitudinal axes (Figure S27b–d, Supporting Information), similarly to the tilt and microfibril angle (MFA) in Geraniaceae seed structures.^[8] Such a demonstrator could also be used to implement rolling motions: we obtained an average rolling speed of 0.4 mm s^{-1} upon 2 locomotion cycles (Figure 3e and Video S6, Supporting Information), yet further investigations on helical radius reduction and boundary conditions to trigger rolling upon coiling are necessary to design rolling systems with enhanced performance.

Taking advantage of the possibility of printing the tracks in different directions on the same BL/PPTL, we have also designed and fabricated a reconfigurable structure devised for uniaxial programmed motion (Figure 3f,g), recalling the uniaxial opening/closing motion of some flowers (e.g., *Carlina aucalis*),^[49] and using the design shown in Figure S27e (Supporting Information).

When exposed to 1 Sun, the considered structure reconfigured its shape in nearly 7 s (Video S7, Supporting Information), and the starting configuration was recovered upon removing the solar stimulus. The dynamic temperature profile caused by irradiation further elucidated the photothermal-hygroscopic actuation strategy introduced in the present demonstrator (Figure 3g.4 and Video S7, Supporting Information).

Overall, and commensurate with the present developmental stage, the reported demonstrators support the potential for effective implementation of the proposed photothermal-hygroscopic actuation strategy in a variety of applications involving soft material systems, and in particular soft actuators.

3. Conclusion

A bioinspired plasmonic photothermal-hygroscopic nanocomposite with AgNPs integrated onto a PDMS surface is here designed and fabricated for the creation of a sunlight-driven (1 Sun) actuator.

An actuator activated by the combination of sunlight and moisture offers a concrete original contribution to the growing quest for actuation systems driven by renewable energy sources, paving the way to develop next-generation soft materials/robotics systems at a sustainable cost.

Thanks to the in situ synthesis, the proposed photothermal-hygroscopic actuators can be obtained through facile fabrication steps involving commonly available materials in the market (e.g., PDMS and AgF for the photothermal effect) and in nature (e.g., cellulose-based materials).

The actuator shows reversible deformation and curvature changes featuring a $\approx 6.8 \pm 0.3$ s response time, associated with a $\approx 43\%$ change in curvature and a 0.76 ± 0.02 mN force under 1 Sun irradiation.

The approach enables a versatile and simple strategy for fabricating soft actuators with more complex designs (grasper, crawler, coiler, lifter, and a light-responsive actuator structure devised for programmed motion) activated by sunlight power.

Compared to the current state of the art in sunlight driven photothermal-humidity actuators, in this work we couple an: 1) in situ, one-step and high-yield synthesis of the plasmonic photothermal agent onto the inactive layer of the actuator with a deep photothermal characterization; 2) anisotropic actuation obtained through controlled alignment of the cellulose tracks printed and aligned similarly *Pelargonium appendiculatum* seed structures; 3) analysis of statics and kinematics properties of the actuation coupled with modeling.

This work provides a useful way for developing a new generation of plasmonic soft actuators for sunlight-driven bioinspired and sustainable soft microrobots actuated by renewable energy sources.

The reported actuator is based on PDMS (as hosting material) that is one of the most used silicon-based elastomers in soft

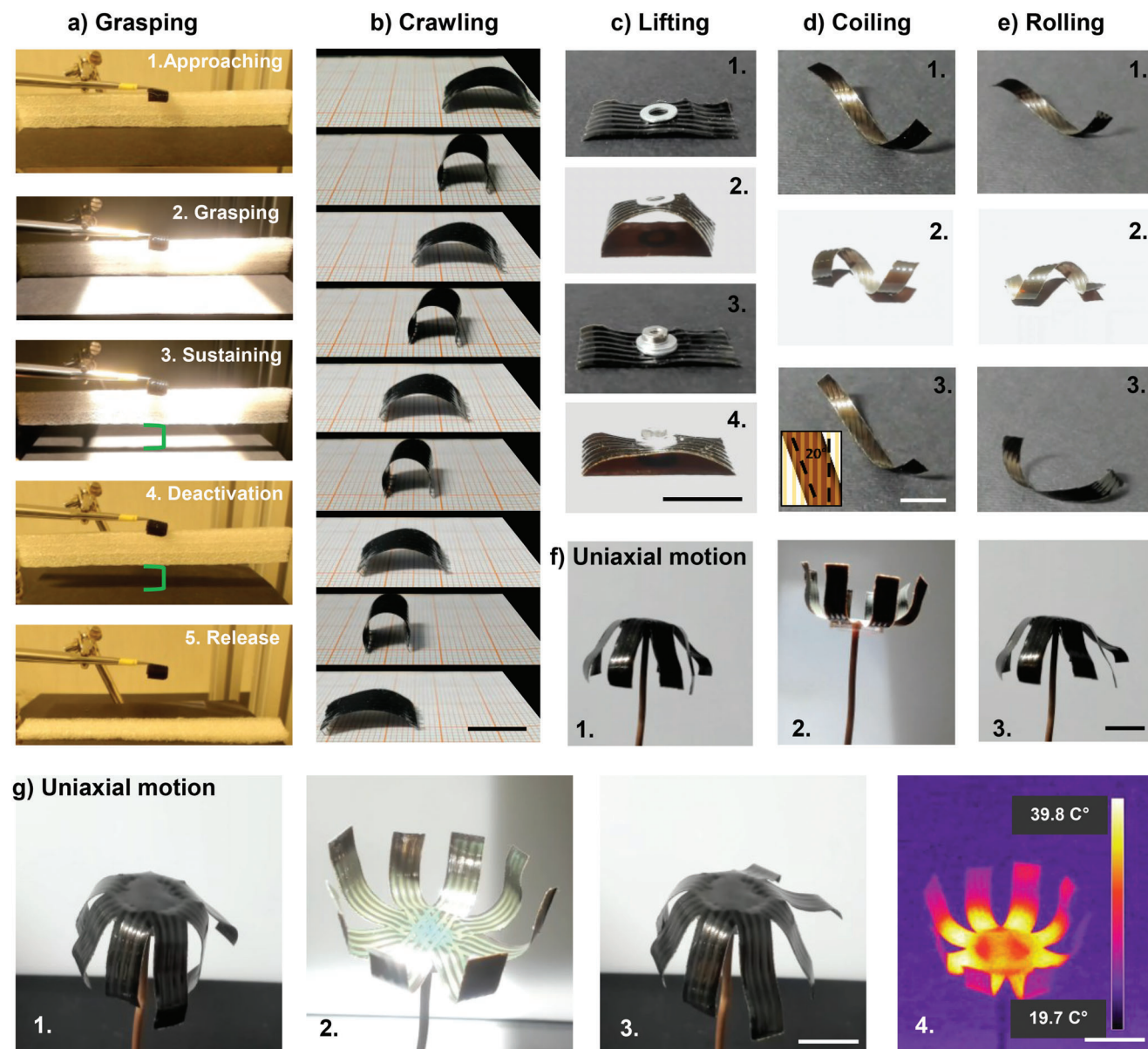


Figure 3. a) Grasping test of a polystyrene sample (156 mg mass \sim 11-fold the actuator mass) with a BL/PPTL/HL rectangular actuator (2×1 cm). The test consists of: 1. Approaching; 2. Grasp activation under light exposure; 3. Sustained grasping; 4. Grasp deactivation; 5. Sample release. b) Crawling test of the rectangular BL/PPTL/HL actuator (2×1 cm) under subsequent light exposure. Scale bar is 2 cm. c) Lifting tests of metallic nuts and washers i.e., 42.6 and 144.1 mg (3-fold and 10-fold the actuator mass, respectively) using a rectangular BL/PPTL/HL actuator (2×1 cm). 1 and 2 show the lifting of the 42.6 mg sample under light exposure while 3 and 4 show the 144.1 mg one. d) Coiling test of a rectangular actuator (0.5×4.5 cm) with CMC tracks printed with an angle of 20° with respect to the longitudinal axis. The pictures show a dark(1)/light exposure(2)/dark(3) cycle. Scale bar is 1 cm. e) Rolling test of the rectangular actuator reported in (d) under dark(1)/light exposure(2)/dark(3) cycles. Scale bar is the same as (d). f,g) Artificial light-responsive actuator structure devised for uniaxial programmed motion based on the BL/PPTL/HL in lateral (f) and tilted view (g) exposed to a dark(1)/light exposure(2)/dark(3) cycle. Scalebar is 1 cm. (4) Thermocamera image during the exposure of the actuator structure devised for uniaxial programmed motion under sunlight. Scale bar is 1 cm. All the experiments are performed under a simulated sunlight power density of 1 Sun.

robotics.^[50] However, the reported fabrication process could be extended to other composites, in which the PDMS layer could be exploited as a coating or hosting material for flat or fibrous reinforcing polymers,^[51] paving the way for a multi-material approach with wider flexibility for soft robotics applications.

A proof of concept of the employment as coating material for deformable structure (i.e., Kapton tape, Polyimide) with a rela-

tively high Young's modulus (2.5 GPa, Figure S28, Supporting Information)^[52] is reported in Video S8 (Supporting Information). The multi-layered composite was reversibly actuated by sunlight with a power density of 1 Sun.

Moreover, based on further calibration of the hygroscopic-photothermal response of the plasmonic nanocomposite, additional applications for sensing could be envisaged. For

instance, considering the self-folding of 2D PDMS-based materials in origami/kirigami 3D structures,^[53] the proposed technology could open new horizons in the fabrication of 3D soft actuators/robots driven by sunlight.

In perspective, the proposed plasmonic nanocomposite technology could be used to actuate also miniature medical end-effectors based on low-intensity (e.g., endoscopic) irradiation, thus complementing the relatively more widespread use of high-intensity laser irradiation in medical applications, such as, e.g., thermal therapy.^[54] Finally, the proposed technology could be used to also develop energy harvesting applications based on photomechanical effects^[55] stimulated by daily environmental variations, as well as bioinspired systems for environmental exploration, including, e.g., artificial seeds able to adaptively explore soils.^[56]

Supporting Information

Supporting Information is available from the Wiley Online Library or from the author.

Acknowledgements

S.M. and L.C. contributed equally to this work. This work had received funding from the European Union Horizon 2020 research and innovation programme under grant agreement No 101017940 (I-Seed), and from the Israeli Ministry of Science and Technology (MOST) Joint Laboratory Israel-Italy (A Plant-Inspired Robot Emulating Decision-Making Abilities of Plants in Dynamical Environments).

Open Access Funding provided by Istituto Italiano di Tecnologia within the CRUI-CARE Agreement.

Conflict of Interest

The authors declare no conflict of interest.

Data Availability Statement

The data that support the findings of this study are available from the corresponding author upon reasonable request.

Keywords

bioinspired and sustainable soft robotics, hygroscopic actuations, photothermal effects, plasmonic nanocomposites, sunlight actuations

Received: April 1, 2023

Published online:

- [1] B. Mazzolai, C. Laschi, *Sci Robot* **2020**, 5, eaba6893.
- [2] F. Hartmann, M. Baumgartner, M. Kaltenbrunner, *Adv. Mater.* **2021**, 33, 2004413.
- [3] C. A. Aubin, B. Gorissen, E. Milana, P. R. Buskohl, N. Lazarus, G. A. Slipher, C. Keplinger, J. Bongard, F. Iida, J. A. Lewis, R. F. Shepherd, *Nature* **2022**, 602, 393.
- [4] S. Poppinga, C. Zollfrank, O. Prucker, J. Rühle, A. Menges, T. Cheng, T. Speck, *Adv. Mater.* **2018**, 30, 1703653.

- [5] C. Dawson, J. F. V. Vincent, A.-M. Rocca, *Nature* **1997**, 390, 668.
- [6] C. J. Eger, M. Horstmann, S. Poppinga, R. Sachse, R. Thierer, N. Nestle, B. Bruchmann, T. Speck, M. Bischoff, J. Rühle, *Adv. Sci.* **2022**, 9, 2200458.
- [7] R. Elbaum, L. Zaltzman, I. Burgert, P. Fratzl, *Science* **2007**, 316, 884.
- [8] Abraham, R. Elbaum, *New Phytol.* **2013**, 199, 584.
- [9] H. S. Atamian, N. M. Creux, E. A. Brown, A. G. Garner, B. K. Blackman, S. L. Harmer, *Science* **2016**, 353, 587.
- [10] S. Taccola, F. Greco, E. Sinibaldi, A. Mondini, B. Mazzolai, V. Mattoli, *Adv. Mater.* **2015**, 27, 1668.
- [11] B. Shin, J. Ha, M. Lee, K. Park, G. H. Park, T. H. Choi, K.-J. Cho, H.-Y. Kim, *Sci Robot* **2018**, 3, eaar2629.
- [12] H. Cheng, Y. Hu, F. Zhao, Z. Dong, Y. Wang, N. Chen, Z. Zhang, L. Qu, *Adv. Mater.* **2014**, 26, 2909.
- [13] D. Van Opdenbosch, G. Fritz-Popovski, W. Wagermaier, O. Paris, C. Zollfrank, *Adv. Mater.* **2016**, 28, 5235.
- [14] F. Zhang, M. Yang, X. Xu, X. Liu, H. Liu, L. Jiang, S. Wang, *Nat. Mater.* **2022**, 21, 1357.
- [15] D. Lunni, M. Cianchetti, C. Filippeschi, E. Sinibaldi, B. Mazzolai, *Adv. Mater. Interfaces* **2020**, 7, 1901310.
- [16] X. Pang, J. Lv, C. Zhu, L. Qin, Y. Yu, *Adv. Mater.* **2019**, 31, 1904224.
- [17] J. Hong, C. Xu, B. Deng, Y. Gao, X. Zhu, X. Zhang, Y. Zhang, *Adv. Sci.* **2022**, 9, 2103926.
- [18] B. Han, Y.-L. Zhang, Q.-D. Chen, H.-B. Sun, *Adv. Funct. Mater.* **2018**, 28, 1802235.
- [19] G. Cai, J. H. Ciou, Y. Liu, Y. Jiang, P. S. Lee, *Sci. Adv.* **2019**, 5, aaw7956.
- [20] Y. Hu, L. Yang, Q. Yan, Q. Ji, L. Chang, C. Zhang, J. Yan, R. Wang, L. Zhang, G. Wu, J. Sun, B. Zi, W. Chen, Y. Wu, *ACS Nano* **2021**, 15, 5294.
- [21] Y. Li, J. Wang, L. Huang, L. Chen, H. Gao, Y. Ni, Q. Zheng, *ACS Sustainable Chem. Eng.* **2022**, 10, 6414.
- [22] H. Zhao, X. Qi, Y. Ma, X. Sun, X. Liu, X. Zhang, M. Tian, L. Qu, *Nano Lett.* **2021**, 21, 8126.
- [23] D. D. Han, Y. L. Zhang, H. B. Jiang, H. Xia, J. Feng, Q. D. Chen, H. L. Xu, H. B. Sun, *Adv. Mater.* **2015**, 27, 332.
- [24] Y. Yang, Y. Liu, Y. Shen, *Adv. Funct. Mater.* **2020**, 30, 1910172.
- [25] Duan, F. Liu, Y. Kong, M. Hao, J. He, J. Wang, S. Wang, H. Liu, Y. Sang, *ACS Appl. Nano Mater.* **2020**, 3, 1002.
- [26] Hu, J. Liu, L. Chang, L. Yang, A. Xu, K. Qi, P. Lu, G. Wu, W. Chen, Y. Wu, *Adv. Funct. Mater.* **2017**, 27, 1704388.
- [27] A. Mourran, H. Zhang, R. Vinokur, M. Möller, *Adv. Mater.* **2017**, 29, 1604825.
- [28] H. Qin, T. Zhang, N. Li, H.-P. Cong, S.-H. Yu, *Nat. Commun.* **2019**, 10, 2202.
- [29] J. Chen, J. Feng, F. Yang, R. Aleisa, Q. Zhang, Y. Yin, *Angew. Chem., Int. Ed.* **2019**, 58, 9275.
- [30] F. Meder, G. A. Naselli, A. Sadeghi, B. Mazzolai, *Adv. Mater.* **2019**, 31, 1905671.
- [31] Y. Wang, E. Sacyani Keneth, A. Kamysnyh, G. Scalet, F. Auricchio, S. Magdassi, *Adv. Mater. Technol.* **2022**, 7, 2101058.
- [32] Z. Li, Z. Ye, L. Han, Q. Fan, C. Wu, D. Ding, H. L. Xin, N. V. Myung, Y. Yin, *Adv. Mater.* **2021**, 33, 2006367.
- [33] Z. Xie, Y. Duo, Z. Lin, T. Fan, C. Xing, L. Yu, R. Wang, M. Qiu, Y. Zhang, Y. Zhao, X. Yan, H. Zhang, *Adv. Sci.* **2020**, 7, 1902236.
- [34] B. Yang, C. Li, Z. Wang, Q. Dai, *Adv. Mater.* **2022**, 34, 2107351.
- [35] S. Mariani, A. A. La Mattina, A. Paghi, L. Strambini, G. Barillaro, *Adv. Funct. Mater.* **2021**, 31, 2100774.
- [36] S. Mariani, M. Corsi, A. Paghi, A. A. La Mattina, L. Strambini, F. P. Frontini, G. Di Giuseppe, G. Barillaro, *Adv. Opt. Mater.* **2021**, 10, 2101610.
- [37] A. K. Jaiswal, A. Hokkanen, M. Kapulainen, A. Khakalo, Nonappa, O. Ikkala, H. Orelma, *ACS Appl. Mater. Interfaces* **2022**, 14, 3315.
- [38] B. Shapiro, E. Smela, *J. Intell. Mater. Syst. Struct.* **2006**, 18, 181.
- [39] <https://nanocomposix.com/pages/silver-nanoparticles-optical-properties>.

- [40] P. Merkl, S. Zhou, A. Zaganariis, M. Shahata, A. Eleftheraki, T. Thersleff, G. A. Sotiriou, *ACS Appl. Nano Mater.* **2021**, *4*, 5330.
- [41] N. Kwon, H. Oh, R. Kim, A. Sinha, J. Kim, J. Shin, J. W. M. Chon, B. Lim, *Nano Lett.* **2018**, *18*, 5927.
- [42] Q. Zhang, J.-J. Xu, Y. Liu, H.-Y. Chen, *Lab Chip* **2008**, *8*, 352.
- [43] S.-U. Victor, V.-B. J. Roberto, in *Silver Nanoparticles* (Ed.: K. Maaz), IntechOpen, Rijeka, **2018**, p. 147, Ch. 8.
- [44] H. Breitenborn, J. Dong, R. Piccoli, A. Bruhacs, L. V. Besteiro, A. Skripka, Z. M. Wang, A. O. Govorov, L. Razzari, F. Vetrone, R. Nac-cache, R. Morandotti, *APL Photonics* **2019**, *4*, 126106.
- [45] J. H. Kim, J.-Y. Hwang, H. R. Hwang, H. S. Kim, J. H. Lee, J.-W. Seo, U. S. Shin, S.-H. Lee, *Sci. Rep.* **2018**, *8*, 1375.
- [46] T. Trantidou, Y. Elani, E. Parsons, O. Ces, *Microsyst. Nanoeng.* **2017**, *3*, 16091.
- [47] C. Li, Q. Li, L. Sun, X. Ye, S. Chen, Z. Wu, J. Huang, W. Wu, X. Jiang, *Opt. Express* **2018**, *26*, 19707.
- [48] S. Timoshenko, *Theory of Plates and Shells*, McGraw Hill, New York **1959**.
- [49] Y. Tahouni, F. Krüger, S. Poppinga, D. Wood, M. Pfaff, J. Rühle, T. Speck, A. Menges, *Bioinspir. Biomim.* **2021**, *16*, 055002.
- [50] E. Sachyani Keneth, A. Kamyshny, M. Totaro, L. Beccai, S. Magdassi, *Adv. Mater.* **2021**, *33*, 2003387.
- [51] R. Ariati, F. Sales, A. Souza, R. A. Lima, J. Ribeiro, *Polymers (Basel)*. **2021**, *13*, 4258.
- [52] <https://www.mit.edu/~6.777/matprops/polyimide.htm>.
- [53] T. van Manen, S. Janbaz, M. Ganjian, A. A. Zadpoor, *Mater. Today* **2020**, *32*, 59.
- [54] E. Redolfi Riva, A. Desii, E. Sinibaldi, G. Ciofani, V. Piazza, B. Mazzolai, V. Mattoli, *ACS Nano* **2014**, *8*, 5552.
- [55] Y.-X. Shi, W.-H. Zhang, B. F. Abrahams, P. Braunstein, J.-P. Lang, *Angew. Chem., Int. Ed.* **2019**, *58*, 9453.
- [56] L. Cecchini, S. Mariani, M. Ronzan, A. Mondini, N. M. Pugno, B. Mazzolai, *Adv. Sci.* **2023**, *10*, 2205146.

ADVANCED MATERIALS TECHNOLOGIES

Supporting Information

for *Adv. Mater. Technol.*, DOI 10.1002/admt.202202166

A Bioinspired Plasmonic Nanocomposite Actuator Sunlight-Driven by a
Photothermal-Hygroscopic Effect for Sustainable Soft Robotics

*Stefano Mariani**, *Luca Cecchini*, *Alessio Mondini*, *Emanuela Del Dottore*, *Marilena Ronzan*,
Carlo Filippeschi, *Nicola Maria Pugno*, *Edoardo Sinibaldi** and *Barbara Mazzolai**

Supporting Information

A bioinspired plasmonic nanocomposite actuator sunlight-driven by a photothermal-hygroscopic effect for sustainable soft robotics

Stefano Mariani,^{1†} Luca Cecchini,^{1;2†} Alessio Mondini,¹ Emanuela Del Dottore,¹ Marilena Ronzan,¹ Carlo Filippeschi,¹ Nicola Maria Pugno,^{2;3} Edoardo Sinibaldi,^{1*} Barbara Mazzolai^{1*}*

¹ Bioinspired Soft Robotics Laboratory, Istituto Italiano di Tecnologia, Via Morego 30, 16163, Genova

² Laboratory for Bioinspired, Bionic, Nano, Meta Materials and Mechanics, Department of Civil, Environmental and Mechanical Engineering, University di Trento, Via Mesiano 77, 38123, Trento

³ School of Engineering and Materials Science, Queen Mary University of London, Mile End Road, E1 4NS, London, United Kingdom

[†] S.M. and L.C. contributed equally to this work

*Emails: stefano.mariani@iit.it; edoardo.sinibaldi@iit.it; barbara.mazzolai@iit.it

Figure S1. State-of-the-art of the photothermal actuators

Section S1. Experimental Section

Figure S2. Preparation of the BL/PPTL/HL actuator

Section S2. Morphological, optical and photothermal characterization of the BL/PPTL

Figure S3. Optical microscope image of the thickness of the PDMS samples

Figure S4. SEM images of the PDMS/AgNPs surface and section

Figure S5. SEM-EDX analysis

Figure S6. Size distribution and coverage of the synthesized AgNPs

Figure S7. Optical characterization of the PDMS/AgNPs surface

Figure S8. Irradiance spectrum of the SciSun300 (ScienceTEC, Canada)

Figure S9. Photothermal characterization of the PDMS/AgNPs surface under 1 Sun irradiation

Figure S10. Photothermal characterization of the PDMS/AgNPs under 0.5, 1 and 1.5 Sun irradiation

Figure S11. Photothermal characterization of the PDMS/AgNPs under 808 nm laser irradiation

Figure S12. Tape tests on PDMS/AgNPs

Figure S13. Contact angle measurements on PDMS samples

Figure S14. SEM image of a PDMS/PVA layer

Figure S15. Photothermal characterization of the PDMS/AgNPs (before and after air plasma)

Section S3. Photothermal conversion efficiency

Section S4. Characterization, kinematic and static of the BL/PPTL/HL actuator

Table S1. Summary of the mechanical properties

Figure S16. Stress/strain test of a PDMS sample.

Figure S17. Sketch of the trilayer composite and its geometrical reference coordinates

Figure S18. Sketch of the experimental setup for force measurement

Figure S19. Prediction of the curvature

Figure S20. Top view optical microscope image of the PDMS/AgNPs/CMC

Figure S21. SEM image of the PDMS/AgNPs/CMC section

Figure S22. Tape tests on PDMS/AgNPs/CMC

Figure S23. Loadcell setup for the measurement of the PDMS/AgNPs/CMC force

Figure S24. Prediction of the maximum force

Figure S25. Non-fatigable reversibility test

Figure S26. Moment comparison with hygroscopic seed

Section S5. Design of the actuators

Figure S27. Design of the grasper, crawler, lifter, coiler, roller and actuator devised for uniaxial programmed motion

Figure S28. Optical image of the Polyimide/Silicone Adhesive/PDMS/AgNPs

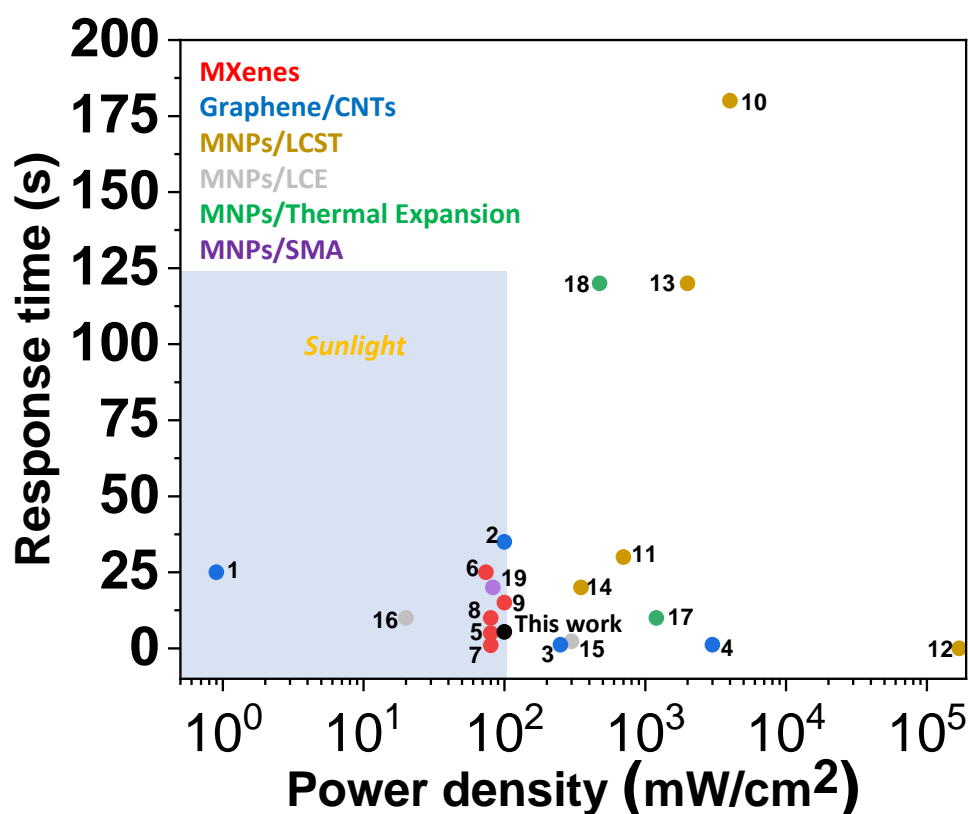


Figure S1. State-of-the-art of photothermal-hygroscopic actuators. For each photothermal agent integrated into an actuator i.e., carbon-based (graphene or CNT),^[1-4] MXene^[5-9] or metal nanoparticles (MNPs)^[9-19] is reported the power density needed (mW/cm²) vs response time (s). The MNP have been further classified according to the material and/or mechanism involved in the actuation (i.e., materials with Lower Critical Solution Temperature (LCST),^[10-14] Liquid Cristal Elastomers or Networks (LCEs or LCNs),^[15,16] materials with thermal expansion,^[17-18] Shape Memory Alloy (SMA). The light-blue region shows the power densities region of solar radiation.^[19]

This work (black bullet) is the first that employs plasmonic only MNPs (i.e., AgNPs) for photothermal/hygroscopic-driven actuation at power densities in the range of solar radiation (1Sun~ 100 mW/cm²).

Section 1 Experimental Section

Materials and chemicals

Silver fluoride (AgF, 99.9%), absolute ethanol (EtOH, 99.9%), Carboxymethyl cellulose (CMC) were purchased from Merck Millipore (Massachusetts, USA). Polyvinyl alcohol (PVA, 98-99% hydrolyzed, high molecular weight) was purchased from ThermoFisher Scientific (Massachusetts, USA). PDMS (polydimethylsiloxane), Sylgard 184 base and thermal curing agent were purchased from Dow Corning Corporation (USA). Deionized water (DIW) was purified by Arium[®] advance EDI (Sartorius, Germany) and filtered using syringe filters (Minisart NML Syringe Filters 1.20 μm , (Sartorius, Germany)).

Preparation of the BL/PPTL/HL actuator

The actuator consisting of PDMS (Base Layer, BL) decorated with silver nanoparticles (AgNPs, Plasmonic Photothermal Layer, PPTL) and Carboxymethyl cellulose (CMC, Hygroscopic Layer, HL), printed by Direct Ink Writing (DIW), was fabricated accordingly with the procedure reported in Figure S2.

PDMS was prepared by mixing base and curing agents (10:1, w:w) and then vacuumed for 30 min using a rotation pump to avoid the formation of air bubbles. Then 0.50g of the mixture was poured into a polystyrene Petri dish (9 cm in diameter) and spin coated (1200 rpm for 60 s). The PDMS was then thermally cured in the oven (VacuTherm, Thermo Scientific, USA) at 80°C for 90 minutes (Figure S2, 1-3). A 20 mM AgF ethanolic solution was used for the synthesis of AgNPs on PDMS. 20 ml of solution was cast in a 9 cm Petri dish for 30, 60, 120, 240, and 360 minutes at room temperature (i.e., 20°C). After decoration, the PDMS/AgNPs in the Petri dish was thoroughly rinsed with ethanol and dried under a gentle nitrogen flow (Figure S2, 4-5).

The PDMS/AgNPs surface was treated with air/oxygen plasma (Tergeo, Pie Scientific, LLC, USA) to increase its hydrophilicity. The plasma time was set to 60s, gas stability time to 15s, power setpoint to 75W, gas setpoint 30 sccm (cm^3/min) and base vacuum to 0.50 mbar (Figure S2, 6).

The activated PDMS/AgNPs surface was spin-coated with PVA (1ml, 1% in DIW, 4000 rpm for 60s), according to the procedure reported in^[20] to stabilize the hydrophilicity PDMS and dried in the oven at 80°C for 15 minutes (Figure S2, 7).

Carboxymethyl cellulose (CMC) was printed via Direct Ink Writing (DIW) using a 3DBioplottter, EnvisionTEC (Germany). CMC hydrogel was prepared in deionized water (10% w/w) under magnetic stirring for 4 hours at 60°C and then vacuumed to remove air bubbles and poured in the 3D Bioplottter nozzle. The CMC was printed directly on the PDMS/AgNPs activated surface using a conical nozzle with a 200 μm diameter and by fixing the printing plate temperature at 25°C. The extrusion pressure was set at 1.7 bar and the printing speed at 33 mm/s. The nozzle offset was fixed at 160 μm for beam samples with a distance between the strands of 1.5 mm. The printed CMC tracks were dried in the oven at 80° for 1 h (Figure S2, 8). Direct-write CO₂ laser (Flux BEAMO, Flux Europe) with tunable laser power, speed, and resolution was then used to cut and pattern the PDMS/AgNPs/CMC surface to fabricate a wide range of soft actuator designs and configurations (Figure S2, 9).

Test rectangle samples (2.0 x 1.0 cm) were cut and peeled off from the Petri dish (Figure S2, 10-11).

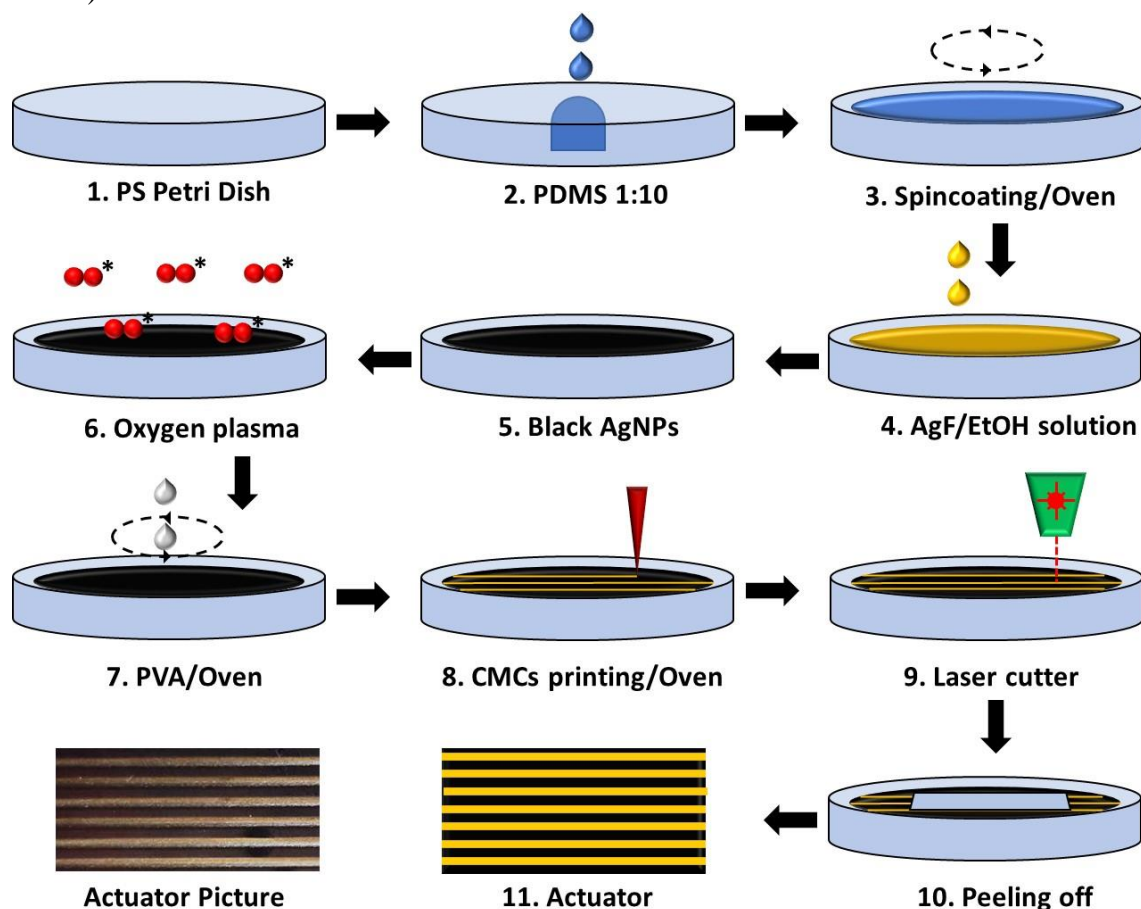


Figure S2. PDMS/AgNPs/CMC actuator preparation protocol. It consists of: (1-3) PDMS mixing and pouring it in a Petri dish, spin-coating and crosslinking in the oven; (4-6) plasmonic Silver Nanoparticles in-situ synthesis using AgF ethanolic solution and oxygen plasma activation; (7) hydrophilic PVA coating via spin-coating and drying in the oven; (8) CMC preparation; (9-11) printing via Direct Ink Writing and drying in the oven, laser cutting and peeling off of the actuators (test samples $1\text{cm} \times 1\text{cm} \times 60\mu\text{m}$).

Surface activation

Contact angle measurements were carried out with an optical tensiometer (Theta OneAttention, Biolin Scientific, Sweden) to evaluate the success of the surface treatments.

Morphological characterization of the PDMS, PDMS/AgNPs and PDMS/AgNPs/CMC surface

Morphological surface characterization was performed using a Helios NanoLab 600i Dual Beam Focused ion beam/field-emission SEM instrument (FEI, USA). The size, distribution, and surface coverage of AgNPs were evaluated by post-processing the images with ImageJ software.^[21] Images of the cross sections were also acquired after cutting with a razor blade. Hirox KH-7700 digital microscope (Japan) was also used for morphological characterization.

Optical characterization of the PDMS/AgNPs surface

Transmittance spectra of the PDMS/AgNPs samples (1cm × 1cm × 50µm), synthesized at different times (30-360 minutes), were collected with a LAMBDA 45 spectrophotometer (Perkin Elmer, USA) in the UV-Vis range (400–1000 nm wavelength).

Reflectance spectra of the PDMS/AgNPs samples, synthesized at different times (30-360 minutes), were collected with a UV-vis-NIR light NanoCalc-XR source and spectrophotometer (Micropack Ocean Optics, USA). Acquisition parameters of the transmittance spectra were: integration time of 1000 ms, average scan number 1, boxcar width 0.

Photothermal characterization of the PDMS/AgNPs surface

Photothermal characterization of the PDMS/AgNPs samples (1cm × 1cm × 50µm), synthesized at different times (30-360 minutes), was carried out with an IR thermal camera (A700, FLIR Systems, USA). The experiments were performed in ambient air (about 20 °C, 60% RH). The samples were irradiated under laser light using RLTM DL-808-1W, 808 nm (Roithner Lasertechnik, Austria), 1 W cw laser at different powers (100-1000 mW) or simulated sunlight using a SciSun 300 Solar Simulator (Sciencetech, Canada) at different powers (50-150 mW/cm², 0.5-1.5 Sun) with intermitting solar irradiation (60s irradiation / 60s of darkness). Power densities of the laser were calculated after the measurement of the power exiting from the fiber with a power meter (Nova II, Ophir, Israel) and the measurement of the irradiated surface with an IR thermal camera (A700, FLIR Systems, USA). Power densities of the simulated sunlight were verified using an RS PRO solar energy meter (RS, UK).

Tape test of the PDMS/AgNPs surface

Tape tests were carried out on the PDMS/AgNPs surface (240 minutes synthesis) to investigate the adhesion properties of the nanoparticles. Tesa® Professional 53988 tape (Germany) tape and the PDMS/AgNPs surface were put in contact applying a pressure of 570 kPa for 1 minute, with a peeling angle of 90°. The tape was then peeled off and the reflectance spectra of the PDMS/AgNPs surface was acquired as reported in *Optical characterization of the PDMS/AgNPs surface* to monitor possible changes due to nanoparticle transfer from PDMS to the tape surface.

Mechanical characterization

We evaluate the stress-strain relation of PDMS/AgNPs (BL/PPTL) synthesized with AgF for 240 minutes and CMC (HL) using a tensile stress test (ZwickRoell Z100). We used a 1kN sensitive load cell, with a speed test of 500 mm/min and 100 mm/min for PDMS/AgNPs and CMC, respectively, and with a pre-load of 0.05N. Young's modulus and Poisson's ratio of PDMS/AgNPs do not give statistically relevant differences with respect to the blank PDMS. The geometrical features of the dumbbell specimens were: length 35 mm, width 4 mm and thickness 50 µm. CMC samples were prepared using the bar coating technique (bar thickness 1mm, speed 20 mm/s) with a DIW solution of 10%wt CMC. Samples were subsequently laser cut in dumbbell specimen shape with geometrical dimensions: length 35mm, width 4 mm, thickness 100 µm.

Tape test of the PDMS/AgNPs/CMC surface

Tape tests were carried out on the PDMS/AgNPs/CMC surface to investigate the adhesion properties of the CMC tracks on the PDMS/AgNPs layer mediated by PVA. Tesa® Professional 53988 tape (Germany) tape, with a tensile strength of 25 N/cm, and the PDMS/AgNPs/CMC surface were put in contact applying a pressure of 570 kPa for 1 minute, with a peeling angle of 90°. The tape was then peeled off and the integrity of the CMC tracks was examined through microscopy with a Hirox KH-7700 (Japan).

Curvature radius measurement

The evaluation of macroscopic geometrical features allowed us to describe the bending deformation, and therefore the kinematics of the actuator. We calculated the relative humidity variation of the curvature in a climatic chamber (CTC256, Memmert GmbH) with the temperature fixed at 30°C. This value was set to guarantee the maximum humidity dynamics of the machine, which ranges from 30% to 90% RH.

After comparing kinematics with modelling results, we were able to determine the curvature time evolution time of the curvature and so, the diffusivity of the cellulose layer. The procedure consisted in: abruptly increase in the humidity level using a water aerosol (from 40% to 80%); the collection of visual data with a camera; data analysis with the software ImageJ^[21]. We used the same approach to evaluate the curvature kinematics and the curvature evolution time when the sample was irradiated by sunlight.

Force measurements

The PDMS/AgNPs/CMC moment was evaluated under %RH increase (from 60% to 90%) and 1 Sun at %RH=60%. In the experimental setup, the samples were in contact with a suspended 10g sensitive load cell (Futek LSB200, USA). The load cell was calibrated (mV vs mN) using samples with a weight force equal to 0.59 mN.

Pictures and video acquisition

Videos and pictures were acquired using Logitech Brio Stream, Logitech (Swiss) and elaborated with Editor Video (Windows).

*Histological analysis of *Pelargonium appendiculatum**

Pelargonium appendiculatum (L.f.) Willd was investigated histologically in the active hygromorphic region of the awn. Following the purchase from Greenmarket di Barbone Valerio (Italy), the awns were cut into 5mm sections to facilitate solvent penetration. Hamann et al.,^[22]

protocol was used as a reference to embed the samples in paraffin. With a Leica SM2010R microtome, 10 µm thick sections were cut, placed on glass slides and deparaffinized. The slices were observed in bright field mode with a Nikon Eclipse Ni-U (Japan) and captured with a DS-Ri2 Nikon camera.

Statistical methods and data analysis

The normality of data distribution was tested with the Shapiro–Wilk test; normally-distributed data were analyzed with ANOVA followed by LSD post hoc with Bonferroni correction and expressed as average \pm standard error. Non-normally distributed data were analyzed with the Kruskal–Wallis test followed by pairwise Wilcox post hoc test with Holm correction and expressed as median \pm 95% confidence interval. Each experiment has been performed in triplicate ($n = 3$), if not differently indicated.

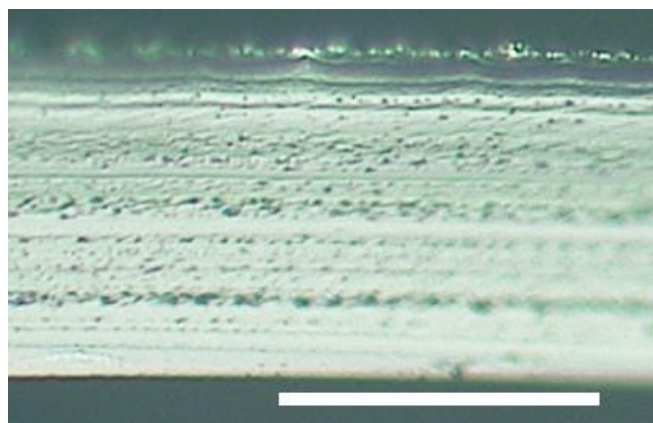
Section 2. Morphological, optical and photothermal characterization of the BL/PPTL

Figure S3. Optical microscope image of the PDMS thickness in the samples. Scalebar is 50 μm .

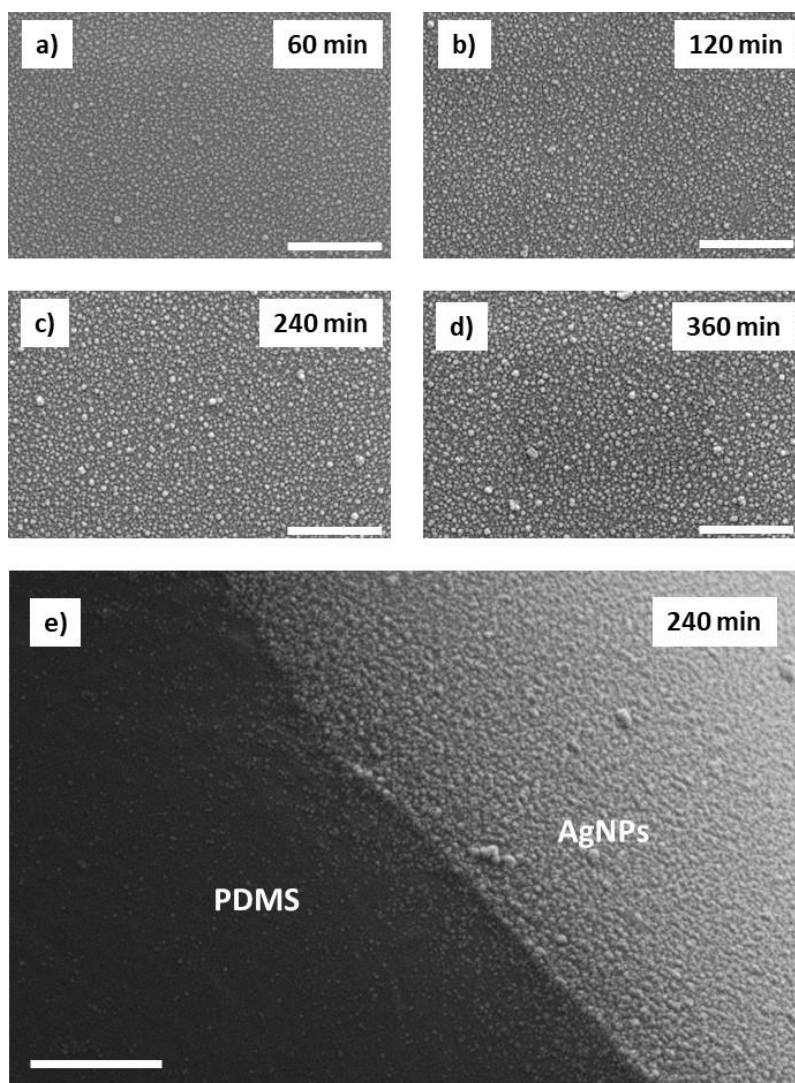


Figure S4. SEM images of the PDMS/AgNPs surface with plasmonic AgNPs synthesized at different times: 60 min (a); 120 min (b); 240 min (c) and 360 min (d). Scalebar is 1 μm . e) Tilted view of the PDMS/AgNPs sample after the 240 min AgNPs synthesis. Scalebar is 1 μm .

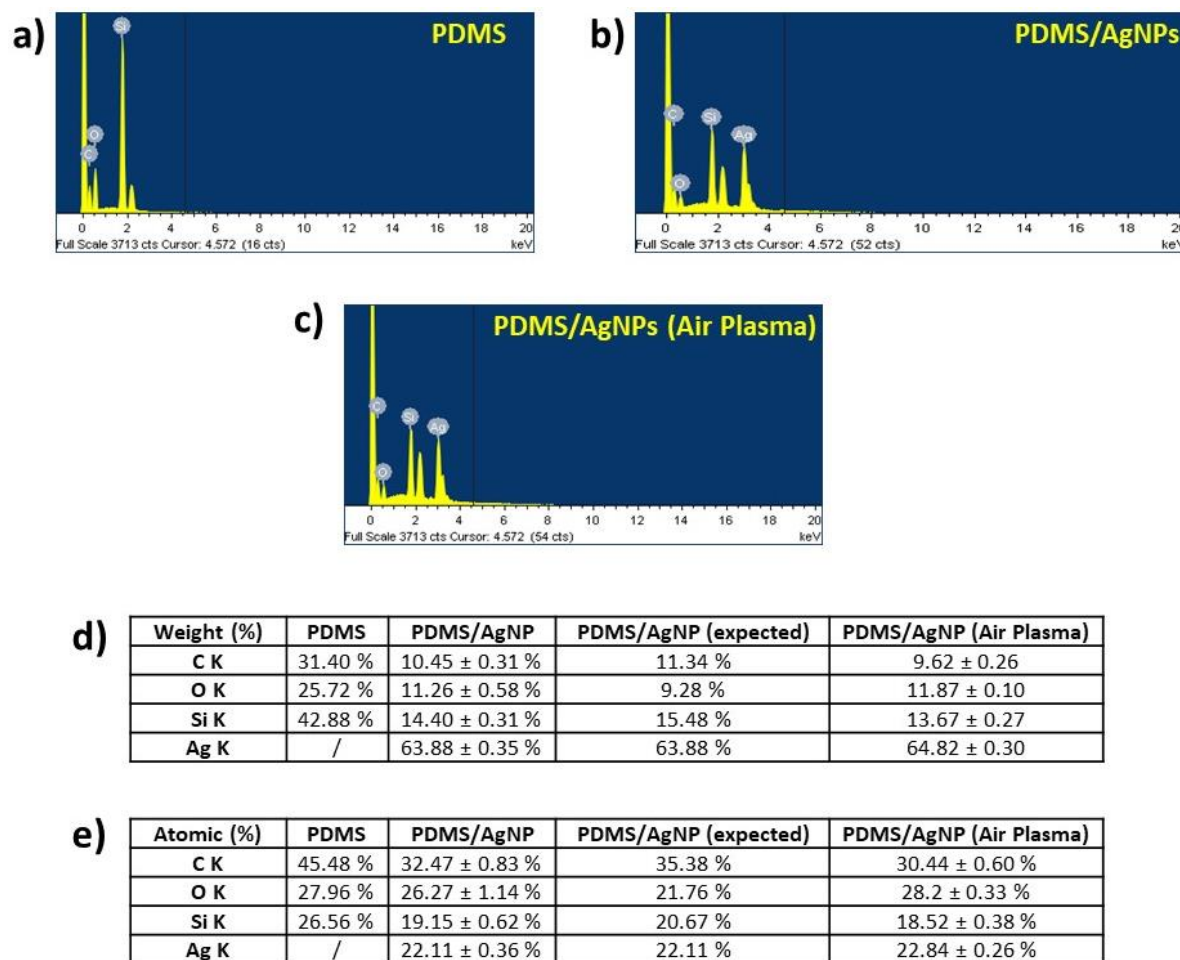


Figure S5. SEM-EDX analysis of the PDMS (a), PDMS/AgNP layer after 240 minutes synthesis, and after the oxidation in air plasma (c). d) and e) show the results (Weight (%) and Atomic (%)) of the analysis reported in images (a-c).

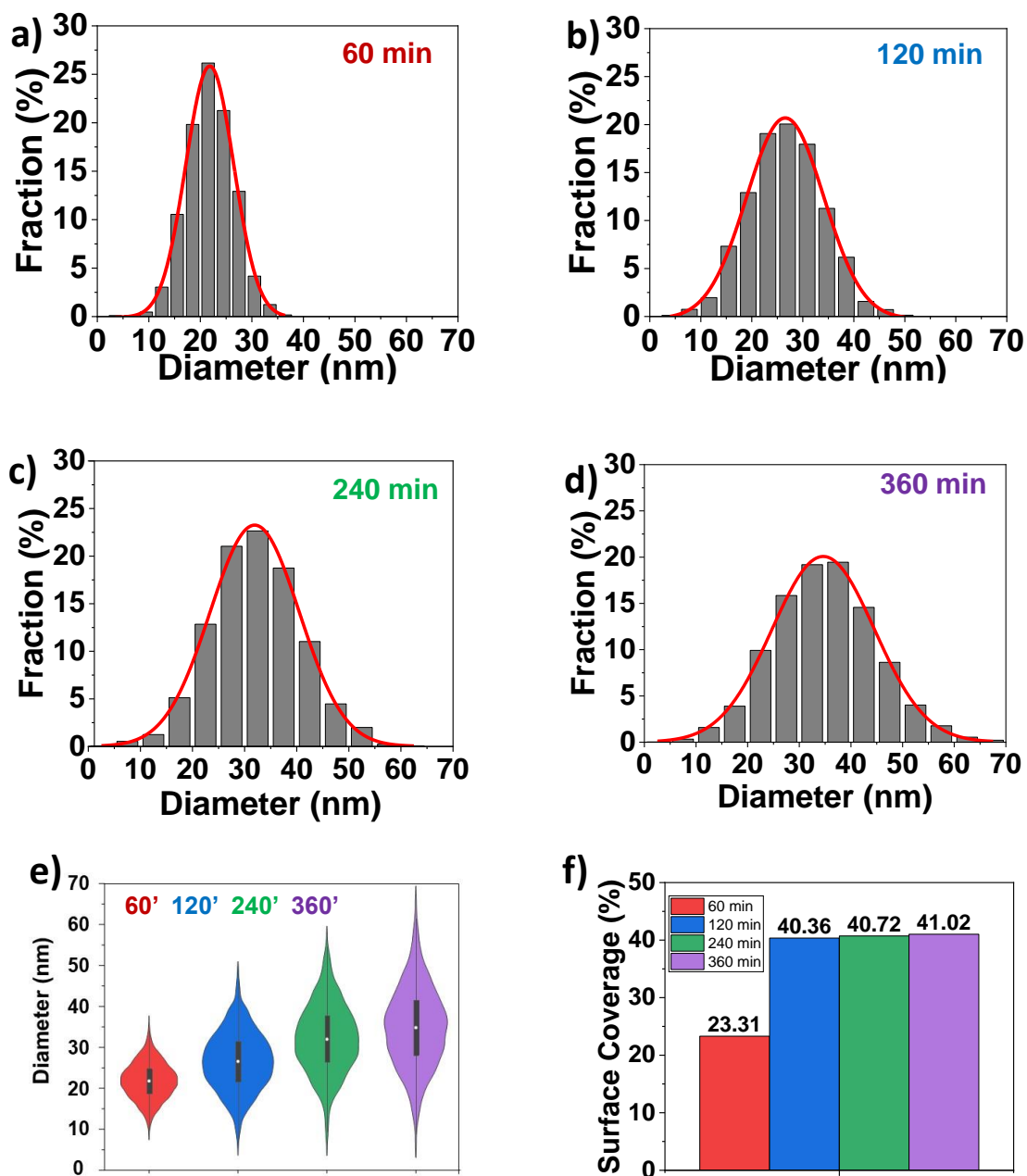


Figure S6. a-d) Size distribution of the plasmonic AgNPs synthesized on the PDMS surface for 60, 120, 240 and 360 minutes. e) Violin plot of the size distribution reported in (a-d). f) Surface coverage of the AgNPs synthesized on the PDMS for 60, 120, 240 and 360 minutes.

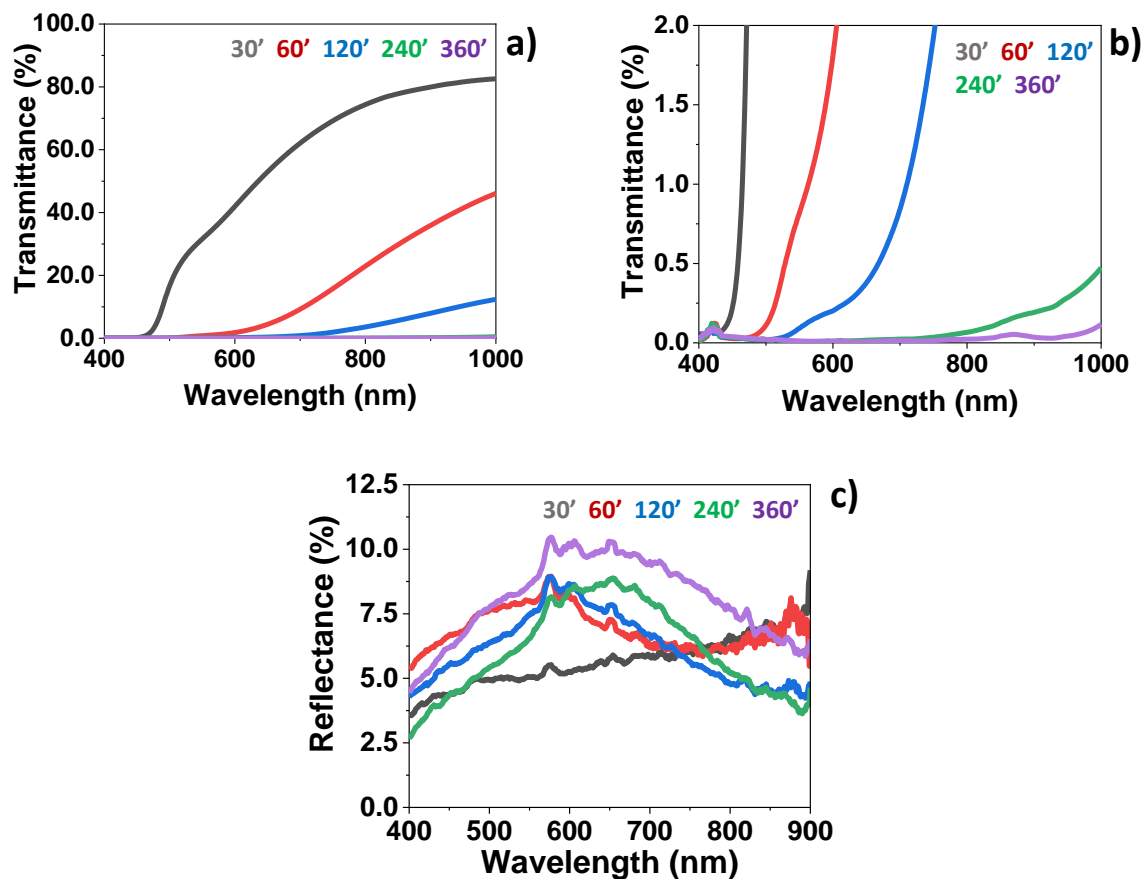


Figure S7. a) Transmittance spectra; b) zoom of the transmittance spectra in (a); c) reflectance spectra of the PDMS/AgNPs surface synthesized for 60, 120, 240 and 360 minutes.

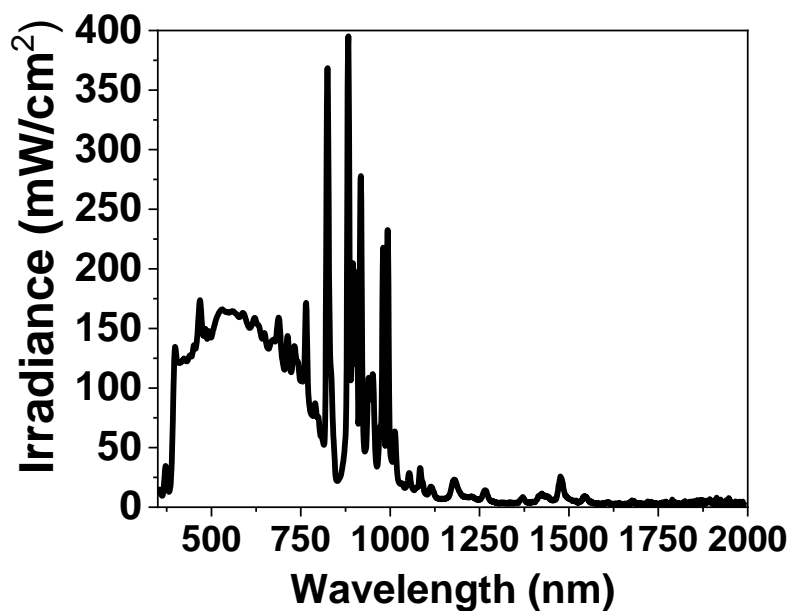


Figure S8. Irradiance spectrum of the SciSun300 (ScienceTEC, Canada)

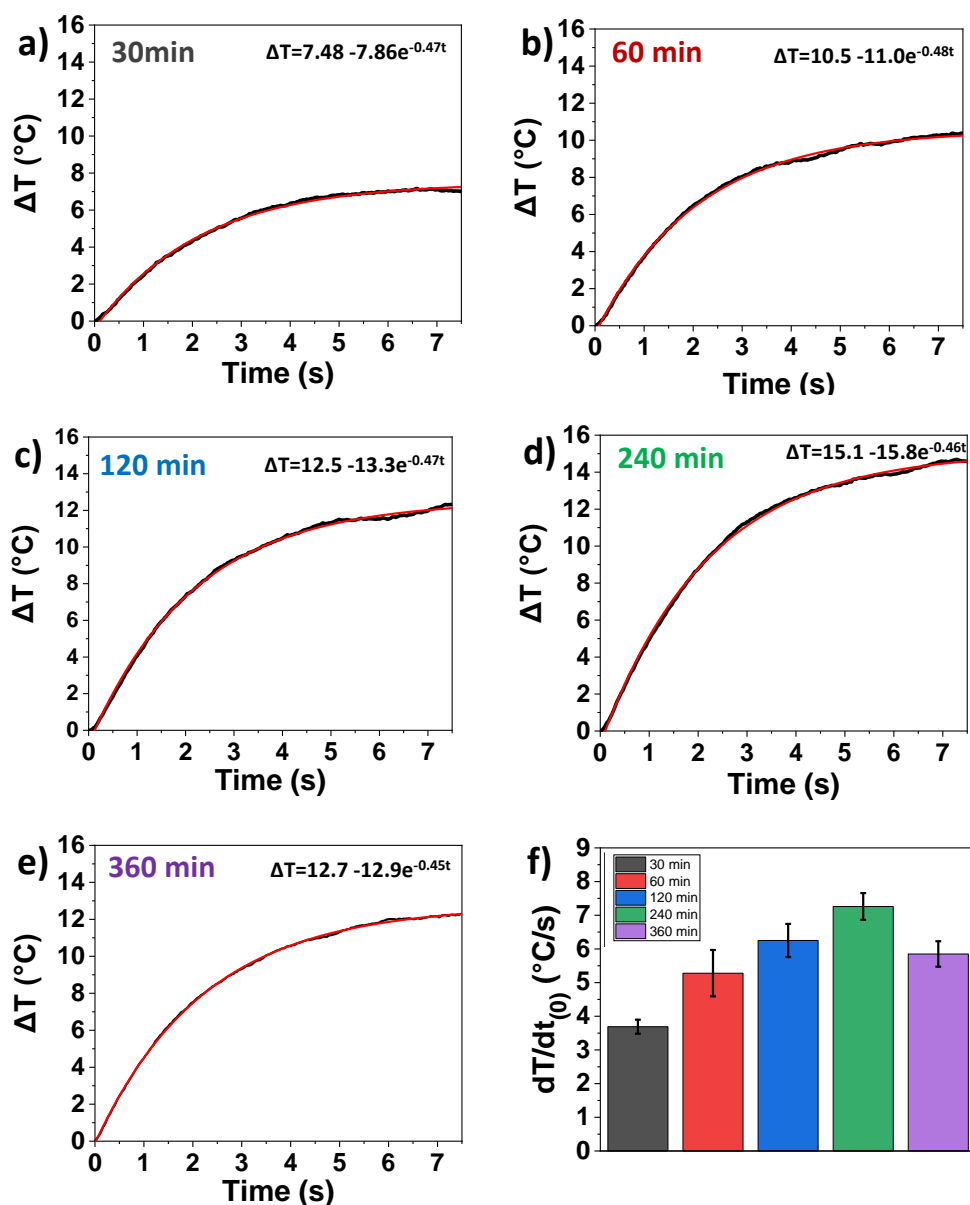


Figure S9. a-f) Exponential fitting of the curves reported in Figure 1g related to the temperature variations (ΔT , °C) over time (s) on the PDMS/AgNPs samples (BL/PPTL) synthesized for 30, 60, 120, 240 and 360 minutes and exposed to a solar simulator light with a power density of 100 mW/cm^2 (1 Sun). The sensitivity $S^{(30)}$, $S^{(60)}$, $S^{(120)}$, $S^{(240)}$ and $S^{(360)}$, respectively computed for 30, 60, 120 and 240 mins of decoration, are:

$$S^{(30)} = d(\Delta T^{(30)})/dt (t=0) = 3.69 \pm 0.21 \text{ °C/s}$$

$$S^{(60)} = d(\Delta T^{(60)})/dt (t=0) = 5.28 \pm 0.69 \text{ °C/s}$$

$$S^{(120)} = d(\Delta T^{(120)})/dt (t=0) = 6.25 \pm 0.49 \text{ °C/s}$$

$$S^{(240)} = d(\Delta T^{(240)})/dt (t=0) = 7.27 \pm 0.40 \text{ °C/s}$$

$$S^{(360)} = d(\Delta T^{(360)})/dt (t=0) = 5.81 \pm 0.38 \text{ °C/s}$$

f) Sensitivity of the curves reported in (a-e) for $t=0$ s. Data are shown as average values \pm SD (N=3).

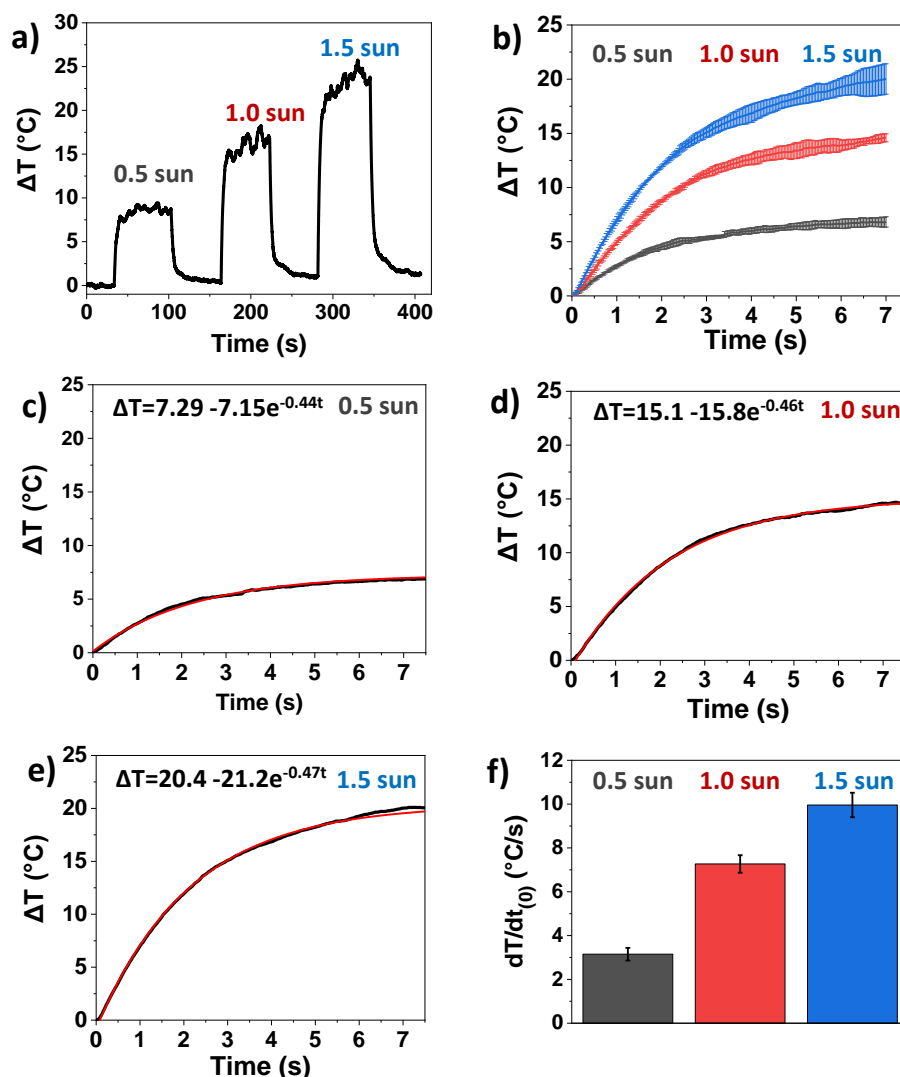


Figure S10. a) Temperature variations (ΔT , °C) over time (s) in a PDMS/AgNPs sample synthesized for 240 min and exposed to a solar light simulator with a power density of 50, 100 and 150 mW/cm^2 (i.e., 0.5, 1 and 1.5 Sun) and with intermitting solar irradiation (60s irradiation / 60s of darkness). b) Three synchronized curves representing the temperature variations (ΔT , °C) over time (s) in a PDMS/AgNPs sample synthesized for 240 min and exposed to a solar light simulator with power densities of 50, 100 and 150 mW/cm^2 over 7 seconds. Data are shown as average values \pm SD (N=3). c-e) Exponential fitting of the curves reported in (b) and related to the temperature variations (ΔT , °C) over time (s) in a PDMS/AgNPs sample synthesized for 240 min and exposed to a solar light simulator with power densities of 50, 100 and 150 mW/cm^2 (i.e., 0.5, 1 and 1.5 Sun).

The sensitivity $S^{(0.5 \text{ Sun})}$, $S^{(1 \text{ Sun})}$ and $S^{(1.5 \text{ Sun})}$, respectively computed for different sunlight exposures, are:

The sensitivity of the curve is a function of the irradiation time.

$$S^{(0.5 \text{ Sun})} = d(\Delta T^{(0.5 \text{ Sun})})/dt (t=0) = 3.15 \pm 0.29 \text{ } ^\circ\text{C}/\text{s}$$

$$S^{(1.0 \text{ Sun})} = d(\Delta T^{(1 \text{ Sun})})/dt (t=0) = 7.27 \pm 0.40 \text{ } ^\circ\text{C}/\text{s}$$

$$S^{(1.5 \text{ Sun})} = d(\Delta T^{(1.5 \text{ Sun})})/dt (t=0) = 9.96 \pm 0.56 \text{ } ^\circ\text{C}/\text{s}$$

f) Sensitivity of the curves reported in (a-e) for $t=0$ s. Data are shown as average values \pm SD (N=3).

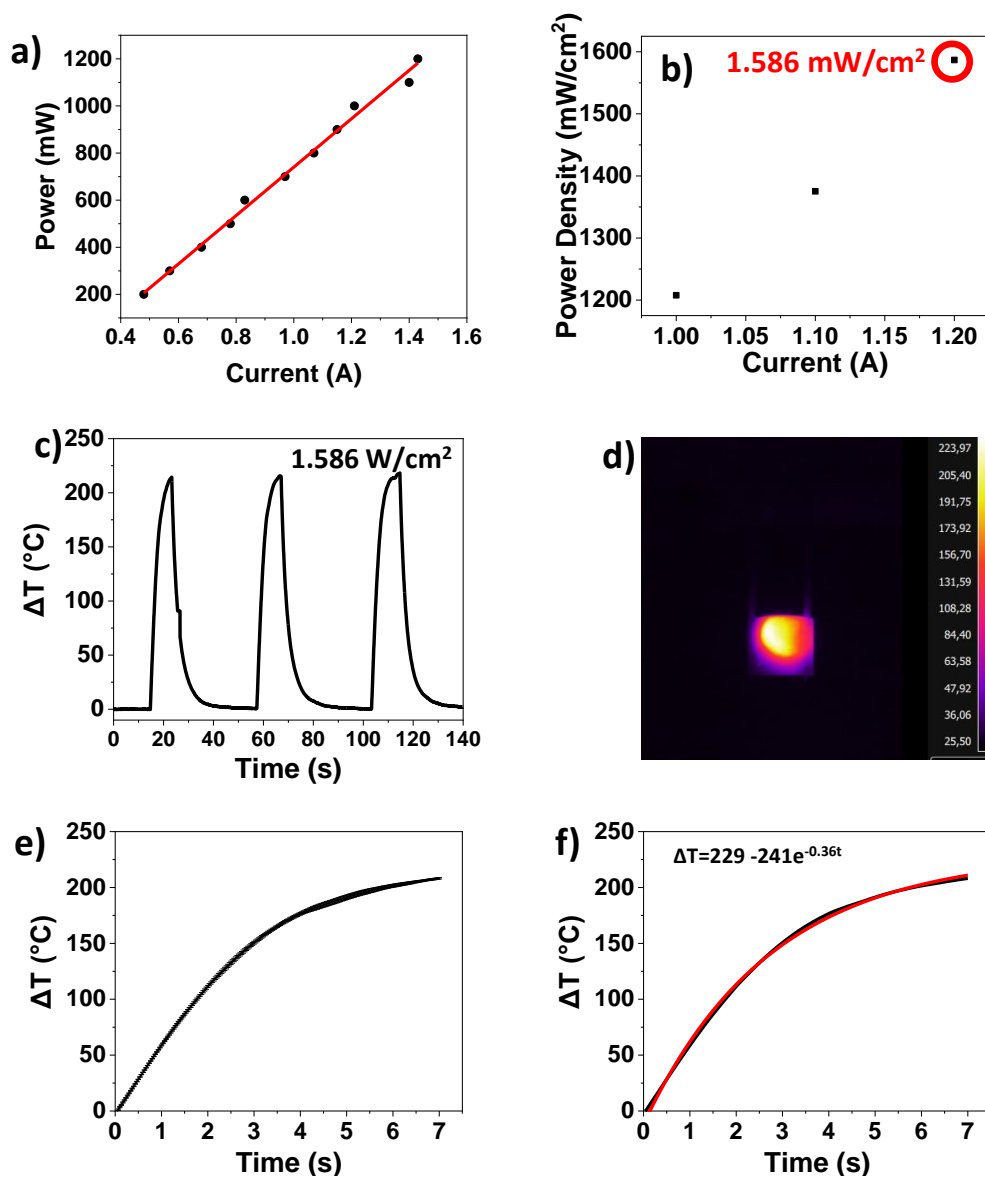


Figure S11. a) Calibration (Current vs theoretical Power) of the RLTM DL-808-1W laser. b) Calibration (Current vs measured Power Density) of the RLTM DL-808-1W laser. 1586 mW/cm^2 is the power density value tested for the photothermal tests reported in (c-f). c) Temperature variations (ΔT , $^{\circ}\text{C}$) over time (s) in a PDMS/AgNPs sample synthesized for 240 min, exposed to a measured laser power density of 1586 mW/cm^2 (3 cycles) and with intermitting laser irradiation (60s irradiation / 60s of darkness). d) Thermocamera images of the PDMS/AgNPs samples during the experiment reported in (c). e) Zoom of (c) considering the first 7 seconds of irradiation (3 synchronized curves). Data are shown as average trend values \pm SD (N=3). f) Exponential fitting of the (e). The sensitivity of the curve is a function of the irradiation time $S = d(\Delta T)/dt$ and it is equal to $86.8 \pm 1.4^{\circ}\text{C}/\text{s}$ for $t=0\text{s}$.

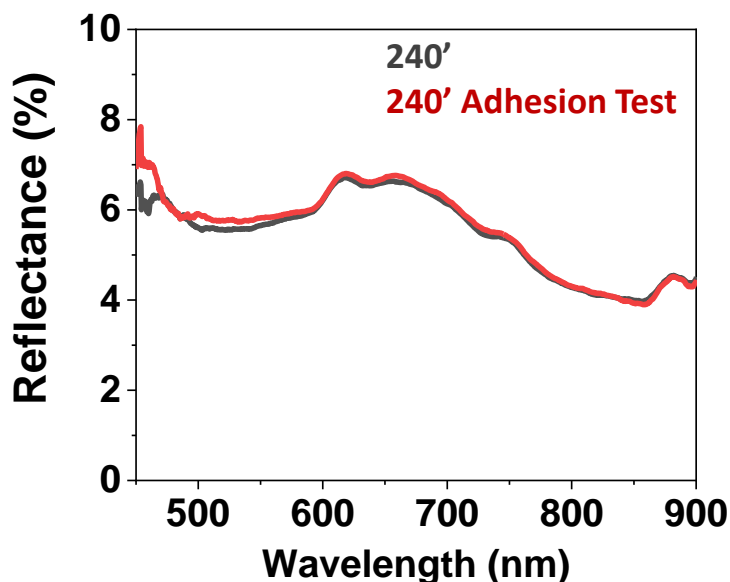


Figure S12. a) Tape tests carried out on a PDMS/AgNPs surface (20 mM AgF:EtOH solution for 240 minutes) using Tesa® Professional 53988 tape with a tensile strength of 25 N/cm and applying a pressure of 570 kPa for 1 minute. The reflectance spectra recorded before test and after tape peeling demonstrate no significant detachment of AgNPs.

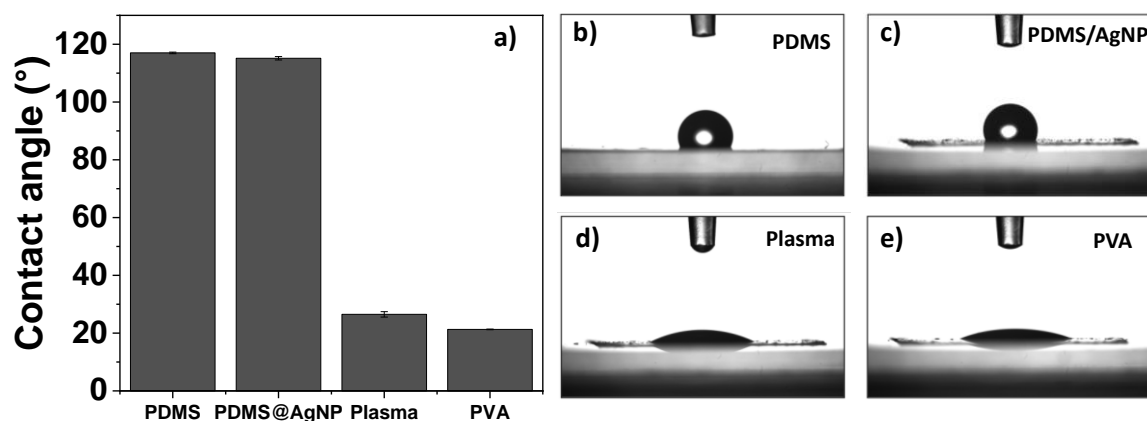


Figure S13. a) Contact angle measurements on the actuator during the different fabrication steps (i.e., PDMS preparation, AgNPs synthesis, plasma treatment and PVA spin-coating with relative water droplet (b-e).

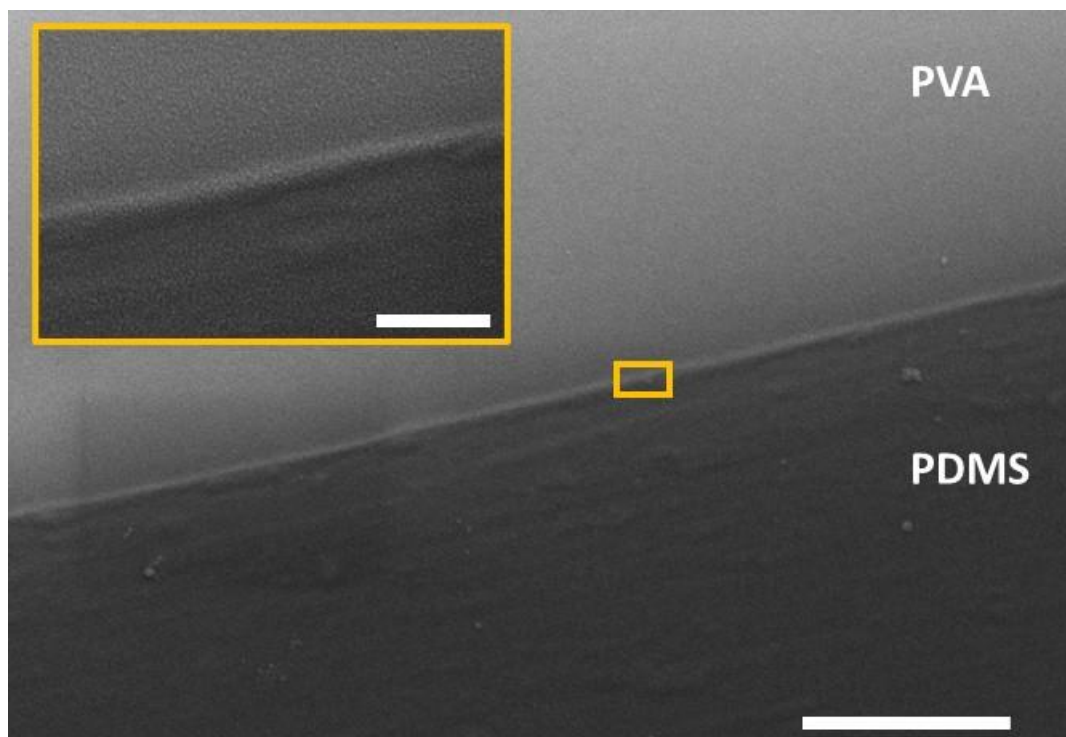


Figure S14. SEM image of a PDMS/PVA layer. Scalebar is 2 μm . Scalebar in the inset in 500 nm.

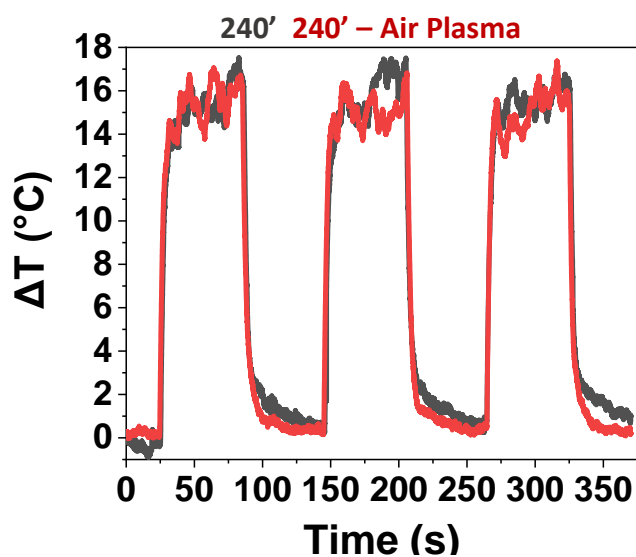


Figure S15. Temperature variations (ΔT , $^{\circ}\text{C}$) over time (s) in a PDMS/AgNPs samples synthesized for 240 min (oxidized with air plasma and not) exposed to intermitting (60s irradiation / 60s of darkness) sunlight irradiation ($100 \text{ mW}/\text{cm}^2$).

Section S3. Photothermal conversion efficiency

Considering the experimental setup, we model the heat transfer of a thin layer structure composed by AgNP photothermal layer on top of PDMS substrate, suspended in air and subjected to surface homogeneous and synchronous irradiation (SUN simulator). The temperature of the body is detected by a thermal camera.

At first, we evaluate the internal conduction problem. Due to homogeneity condition, we assume that the surface of the structure is coherently at the same temperature. This permits to reduce the problem from 3D to 1D. Let's consider a one-dimensional uniform and isotropic PDMS layer, with a thermal source on the top of the surface (AgNP layer). The heat equation is then described as:

$$\begin{aligned} \frac{\partial T(x, t)}{\partial t} &= \frac{k}{\rho c_p} \frac{\partial^2 T(x, t)}{\partial x^2} & t \in [0, +\infty) \quad x \in [0, L] \\ T(0, t) &= T_s(t) & t \in [0, +\infty) \\ T(x, 0) &= T_0 & x \in (0, L] \end{aligned}$$

where T is the temperature, x the thickness length, L the thickness of the PDMS layer, t the time, k the thermal conductivity of PDMS, ρ the density of PDMS, c_p the specific heat capacity of PDMS, $T_s(t)$ the temperature of the AgNP surface as function of time and T_0 the initial temperature of the body (ambient temperature). Therefore, we determine the thermal diffusion time τ :

$$\tau = L^2 \frac{\rho c_p}{4 k}$$

Considering the PDMS data ($\rho = 0.97 \frac{kg}{m^3}$, $c_p = 1.46 \frac{kJ}{kg K}$, $k = 0.15 \frac{W}{m K}$, $L = 55 \mu m$), we obtain that $\tau = 5.9 \mu s$. The experimental dynamic range of the photothermal conversion efficiency (characteristic time 2.17s Fig.S10) is six orders of magnitude higher with respect to diffusion time, so we can assume isothermal conditions in the structure (thin film approximation).

It is now possible to evaluate the photothermal conversion efficiency considering the law of conservation of energy. We model the body as a 2D isothermal horizontal plate, heated by irradiation (photothermal property), which exchange heat with atmospheric air in natural convection regime (infinite reservoir at constant temperature T_{Air}). The heat transfer can be written as:

$$\begin{aligned} \frac{\partial Q_r(\lambda)}{\partial t} - \frac{\partial Q_c}{\partial t} &= \sum_i^N m_i c_{p_i} \frac{\partial T_i}{\partial t} = \frac{\partial T}{\partial t} m c_p \\ m c_p &= \sum_i^N m_i c_{p_i} \end{aligned}$$

where Q_r is the irradiation heat, Q_c is the convection heat, m the mass, c_p the specific heat capacity, T the temperature and t the time.

The convection heat transfer for a 2D isothermal plate is defined as:

$$\frac{\partial Q_c}{\partial t} = h S [T(t, \lambda) - T_{Air}]$$

Where h is the average heat transfer coefficient, S the surface exposed to atmospheric air. We model the irradiation heat transfer according to the Beer-Lambert law:

$$\frac{\partial Q_r(\lambda)}{\partial t} = \eta(\lambda) I_0(\lambda) (1 - 10^{-\alpha(\lambda)})$$

Where η is the photothermal convection efficiency, defined as the ratio of thermal power (extinction) over the absorbed optical power (absorption), I_0 the optical power, α the absorbance and λ the wavelength of the impinging light source.

Finally, we obtain the equation:

$$\frac{\partial T(t, \lambda)}{\partial t} = \eta(\lambda) \frac{I_0(\lambda) (1 - 10^{-\alpha(\lambda)})}{m c_p} - \frac{h S}{m c_p} [T(t, \lambda) - T_{Air}]$$

Considering T_0 as an arbitrary initial temperature, the non-homogeneous linear ordinary differential equation admits a solution equal to:

$$T(t, \lambda) = T_{Air} + \frac{A(\lambda)}{B} (1 - e^{-Bt}) + (T_0 - T_{Air}) e^{-Bt}$$

$$A(\lambda) = \eta(\lambda) \frac{I_0(\lambda) (1 - 10^{-\alpha(\lambda)})}{m c_p}$$

$$B = \frac{h S}{m c_p}$$

Hence, we used the experimental results of temperature kinetics to fit A and B considering the characteristic time $\tau = 1/B$ and the variation of temperature $\Delta T = A/B$.

The PCE is finally evaluated as:

$$\eta(\lambda) = A(\lambda) \frac{m c_p}{I_0(\lambda) (1 - 10^{-\alpha(\lambda)})} = \frac{\Delta T(\lambda)}{\tau(\lambda)} \frac{\rho_1 c_{p_1} t_1 + SC \rho_2 c_{p_2} t_2}{J_0(\lambda) (1 - 10^{-\alpha(\lambda)})}$$

Where ρ is the density, t the thickness, J_0 the optical power density, 1 and 2 refer to PDMS and AgNPs materials, respectively, SC the surface coverage of AgNPs.

It is now important to note that for each wavelength of the input light source there is a unique value of $A(\lambda)$, and so a unique solution of the PCE.

We then calculated the PCE for a single reference value of wavelength by using an 808nm laser source. Then we compared the results with an average value of the PCE assuming a constant 1 Sun of solar irradiance for the whole spectrum of the SUN simulator (window function from 400nm to 900nm of wavelength).

We assumed:

- 1) PDMS: density = 0.97 kg/m^3 specific heat capacity = 1460 J/kg K
- 2) AgNP: density = 10490 kg/m^3 specific heat capacity = 235 J/kg K

For the sample with 4h of AgNPs decoration, we obtained:

- I) PCE@808nm: 41.7%
- II) PCE@SUN: 40.8%

Section S4. Characterization, kinematic and static of the BL/PPTL/HL actuator

The analytical solution of static deformation in a multi-layered composite can be modeled by means of a Timoshenko beam model^[28] (sandwich composite beams), or by using a Laminate composite plates model.^[29]

Considering a purely elastic composite, the constitutive relation for strain ϵ due to bending is assumed to be linear along the height variable z :

$$\epsilon(z) = \epsilon_0 + \kappa z \quad (1)$$

where ϵ_0 (unknown) is the strain at the bottom plane $z = 0$, and κ (unknown) is the bending curvature of the beam.

The stress σ is expressed as:

$$\sigma = \sum_i \mathbf{D}_i (\epsilon(z) - \epsilon_{h_i}) \quad (2)$$

where i represents the i -th layer, \mathbf{D}_i the material stiffness and ϵ_h the hygroscopic strain associated to the i -th layer, modeling the hygroscopic driving effect as detailed below. Let us remark that, as for the curvature computation, the choice of the reference plane is immaterial (based on the assumed linear trend of ϵ versus z for thin plate deformation).

Supposing that the hygroscopic expansion be linear with respect to the relative humidity variation, the hygroscopic strain is modeled as:

$$\epsilon_h = \alpha \Delta \Phi = \alpha [\Phi - \Phi_0] \quad (3)$$

where α is the linear coefficient of hygroscopic expansion, Φ is the relative humidity and Φ_0 is the value of relative humidity at which the mechanical system shows a curvature $\kappa = \mathbf{0}$. To calibrate the considered model, Φ_0 must be evaluated experimentally (as a working parameter accounting for, e.g., residual stresses and structural imperfections resulting from fabrication).

Considering the force \mathbf{F} and moment \mathbf{M} per unit width in equilibrium and in absence of external (domain $z \in [0, h]$, where h is the total thickness of the beam), we obtain:

$$\mathbf{F} = \sum_i \int_{t_i}^{t_{i+1}} \mathbf{D}_i (\epsilon_0 + \kappa z) dz - \Delta \Phi \sum_i \int_{t_i}^{t_{i+1}} \mathbf{D}_i \alpha_i dz = 0 \quad (4)$$

$$\mathbf{M} = \sum_i \int_{t_i}^{t_{i+1}} \mathbf{D}_i (\epsilon_0 + \kappa z) z dz - \Delta \Phi \sum_i \int_{t_i}^{t_{i+1}} \mathbf{D}_i \alpha_i z dz = 0 \quad (5)$$

For sake of compactness, we can report the previous equations in matrix form as:

$$\begin{pmatrix} \epsilon_0 \\ \kappa \end{pmatrix} = \Delta\Phi \begin{bmatrix} \mathbf{A} & \mathbf{B} \\ \mathbf{B} & \mathbf{C} \end{bmatrix}^{-1} \begin{pmatrix} \mathbf{U} \\ \mathbf{V} \end{pmatrix} \quad (6)$$

where \mathbf{U} is the hygroscopic force vector per unit RH, \mathbf{V} the hygroscopic moment vector per unit RH, \mathbf{A} the extensional stiffness, \mathbf{B} the coupling stiffness and \mathbf{C} the bending stiffness, analytically defined as:

$$\mathbf{A} = \sum_i \mathbf{D}_i (z_{i+1} - z_i)$$

$$\mathbf{B} = \frac{1}{2} \sum_i \mathbf{D}_i (z_{i+1}^2 - z_i^2)$$

$$\mathbf{C} = \frac{1}{3} \sum_i \mathbf{D}_i (z_{i+1}^3 - z_i^3)$$

$$\mathbf{U} = \sum_i \mathbf{D}_i \alpha_i (z_{i+1} - z_i)$$

$$\mathbf{V} = \frac{1}{2} \sum_i \mathbf{D}_i \alpha_i (z_{i+1}^2 - z_i^2)$$

According to the theory of laminate composite plates, the \mathbf{D} is the stiffness matrix is defined as:

$$\mathbf{D} = \frac{E}{1 - \nu^2} \begin{pmatrix} 1 & \nu & 0 \\ \nu & 1 & 0 \\ 0 & 0 & \frac{1 - \nu}{2} \end{pmatrix}$$

where E is the Young's modulus and ν the Poisson's ratio. Moreover, Timoshenko beam model is a limit case of the laminate composite plates in which $\nu \rightarrow 0$.

Considering now the trilayered structure at hand (with layers sequentially bounded by $t_0 = 0, t_1 = h_1, t_2 = h_1 + h_2, t_3 = h_1 + h_2 + h_3$), and recalling that both Timoshenko and Laminated composite plates model assume a uniform thickness or the involved layers, we first homogenize the cellulose layer as sketched in Figure S17, the effective cellulose thickness \tilde{h}_{CMC} is:

$$h_{CMC} = \tilde{h}_{CMC} \frac{w_{CMC}}{w_{CMC} + w_{Empty}}$$

We then computed the solution both by assuming a negligible Poisson effect (Timoshenko composite beam model) and by including the Poisson effect (Laminate Composite Plates model), as detailed below.

Timoshenko trilayer model

Solving the equations (6) with $v=0$, we finally obtain:

$$A = E_1 h_1 + E_2 h_2 + E_3 h_3 = E_1 h_1 (1 + m_2 n_2 + m_3 n_3)$$

$$\begin{aligned} B &= \frac{1}{2} (E_1 h_1^2 + E_2 (h_2^2 + 2 h_1 h_2) + E_3 (h_3^2 + 2 h_1 h_3 + 2 h_2 h_3)) \\ &= \frac{1}{2} E_1 h_1^2 (1 + m_2 (n_2^2 + 2 n_2) + m_3 (n_3^2 + 2 n_3 + 2 n_2 n_3)) \end{aligned}$$

$$\begin{aligned} C &= \frac{1}{3} (E_1 h_1^3 + E_2 (h_2^3 + 3 h_1^2 h_2 + 3 h_1 h_2^2) + E_3 (h_3^3 + 3 h_1^2 h_2 + 3 h_1 h_2^2 + 3 h_2^2 h_3 + 3 h_2 h_3^2 \\ &\quad + 6 h_1 h_2 h_3)) \\ &= \frac{1}{3} E_1 h_1^3 (1 + m_2 (n_2^3 + 3 n_2 + 3 n_2^2) + m_3 (n_3^3 + 3 n_2 + 3 n_3^2 + 3 n_2^2 n_3 \\ &\quad + 3 n_2 n_3^2 + 6 n_2 n_3)) \end{aligned}$$

$$U = \alpha_3 E_3 h_3 = \alpha_3 E_1 h_1 (m_3 n_3)$$

$$V = \frac{1}{2} \alpha_3 E_3 (h_3^2 + 2 h_1 h_2 + 2 h_2 h_3) = \frac{1}{2} \alpha_3 E_1 h_1^2 m_3 (n_3^2 + 2 n_2 + 2 n_2 n_3)$$

where:

$$\begin{aligned} m_2 &= \frac{E_2}{E_1} & m_3 &= \frac{E_3}{E_1} \\ n_2 &= \frac{h_2}{h_1} & n_3 &= \frac{h_3}{h_1} \end{aligned}$$

The resulting curvature finally reads:

$$\beta = 6 m_3 n_3 (1 + m_3 + m_2^2 n_2 + m_2 (2 + m_3 n_2))$$

$$\begin{aligned} \gamma &= 1 + m_2^4 n_2^2 + 4 m_3 n_3 + 6 m_3^2 n_3 + 4 m_3^3 n_3 + m_3^4 n_3^2 + 4 m_2^3 (n_2 + m_3 n_2 n_3) \\ &\quad + 6 m_2^2 (n_2 + 2 m_3 n_3 + m_3^2 n_2 n_3) + 4 m_2 (n_2 + 3 m_3 (1 + m_3) n_3 + m_3^3 n_2 n_3) \end{aligned}$$

$$\xi = \frac{\beta}{\gamma} \quad , \quad \kappa = \frac{\alpha_3}{h_1} \xi$$

as previously reported from Shapiro et Smela^[28].

Laminate composite plates

The model at hand considers the deformation u_{xx} along the CMC fiber direction (x), as well as the orthogonal deformation u_{yy} along the transversal direction (y) and the complementary shear deformation u_{xy} . Hence, each element of the matrix system (6) is described by the reference pseudovector:

$$\mathbf{u} = \begin{pmatrix} u_{xx} \\ u_{yy} \\ u_{xy} \end{pmatrix}$$

From Eq.6 the curvature vector $\boldsymbol{\kappa} = (\kappa_x \ \kappa_y \ \kappa_{xy})^T$ can be transformed in the matrix form:

$$\mathbf{b} = \begin{pmatrix} \kappa_{xx} & \kappa_{xy} \\ \kappa_{xy} & \kappa_{yy} \end{pmatrix}$$

From the Kirchoff's theory of thin plates, the maximum eigenvalue of the curvature tensor \mathbf{b} represents the principal curvature κ_0 . The resulting curvature is calculated numerically using Matlab script (Mathworks).

Experimental Static force estimate

Based on the modeling approach, we aimed to estimate the actuation force F_b recorded through the related experiment. Specifically, starting from an initial RH value Φ_i , associated with an equilibrium curvature $\boldsymbol{\kappa}_i$, we assumed to increase RH up to a final value Φ_f while blocking the curvature (so that $\boldsymbol{\kappa}_f = \boldsymbol{\kappa}_i$, systematically) through a pure moment. We introduced such a simplification, compared to the experimental conditions, to straightforwardly compute a blocking moment \mathbf{M}_b from the force and moment equilibrium, as follows:

$$F = \sum_i \int_{t_i}^{t_{i+1}} \mathbf{D}_i (\boldsymbol{\epsilon}_0 + \boldsymbol{\kappa}_i z) dz - \Delta\Phi_f \sum_i \int_{t_i}^{t_{i+1}} \mathbf{D}_i \boldsymbol{\alpha}_i dz = 0 \quad (7)$$

$$\mathbf{M}_b = \sum_i \int_{t_i}^{t_{i+1}} \mathbf{D}_i (\boldsymbol{\epsilon}_0 + \boldsymbol{\kappa}_i z) z dz - \Delta\Phi_f \sum_i \int_{t_i}^{t_{i+1}} \mathbf{D}_i \boldsymbol{\alpha}_i z dz \quad (8)$$

More in detail, in Eq. (7) $\boldsymbol{\kappa}_i$ and $\Delta\Phi_f = \Phi_f - \Phi_0$ are given, so that we can obtain $\boldsymbol{\epsilon}_0$ and, after substitution into Eq. (8), we can finally obtain the blocking moment as follows:

$$\mathbf{M}_b = (\mathbf{C} - \mathbf{B} \mathbf{A}^{-1} \mathbf{B}) \boldsymbol{\kappa}_i + (\mathbf{B} \mathbf{A}^{-1} \mathbf{U} - \mathbf{V}) \Delta\Phi$$

where relevant definitions for the coefficients are recalled from above. In the considered plane problem, we ended up with a single moment component, hereafter denoted as M_b . Considering the schematic in (Figure S18), we then estimated the recorded force F_b as follows:

$$\theta = \frac{l}{2} \kappa$$

$$F_b \cong M_b \frac{\kappa}{\sin\left(\frac{l\kappa}{2}\right)} \quad (9)$$

Clearly, we introduced several simplifications. We neglected membrane and shear forces, and we estimated F_b in Eq. (9) by assuming that M_b suitably approximates the moment in at mid sample. Overall, therefore, the above simplifications were regarded to as working assumptions, deliberately introduced to directly leverage the analytical framework provided by Eq. (7), Eq. (8) (i.e., Eq. (4), Eq. (5)), and to be possibly refined based on comparison with the experimental results.

	PDMS/AgNPs	PVA	CMC
Young's Modulus	1.95 ± 0.34 MPa	2 GPa ^[24]	22.32 ± 2.35 MPa
Poisson's ratio	0.5±0.01	0.44 ^[25]	0.32±0.05
CHE	0	0	0.01-0.1 ^[26, 27]
Thickness	50 μm	60 nm	13.5 μm
Width	1 cm	1 cm	1 cm
Length	2 cm	2 cm	2 cm

Table S1. Summary of experimental and literature mechanical properties of the materials involved in the making of the actuator.

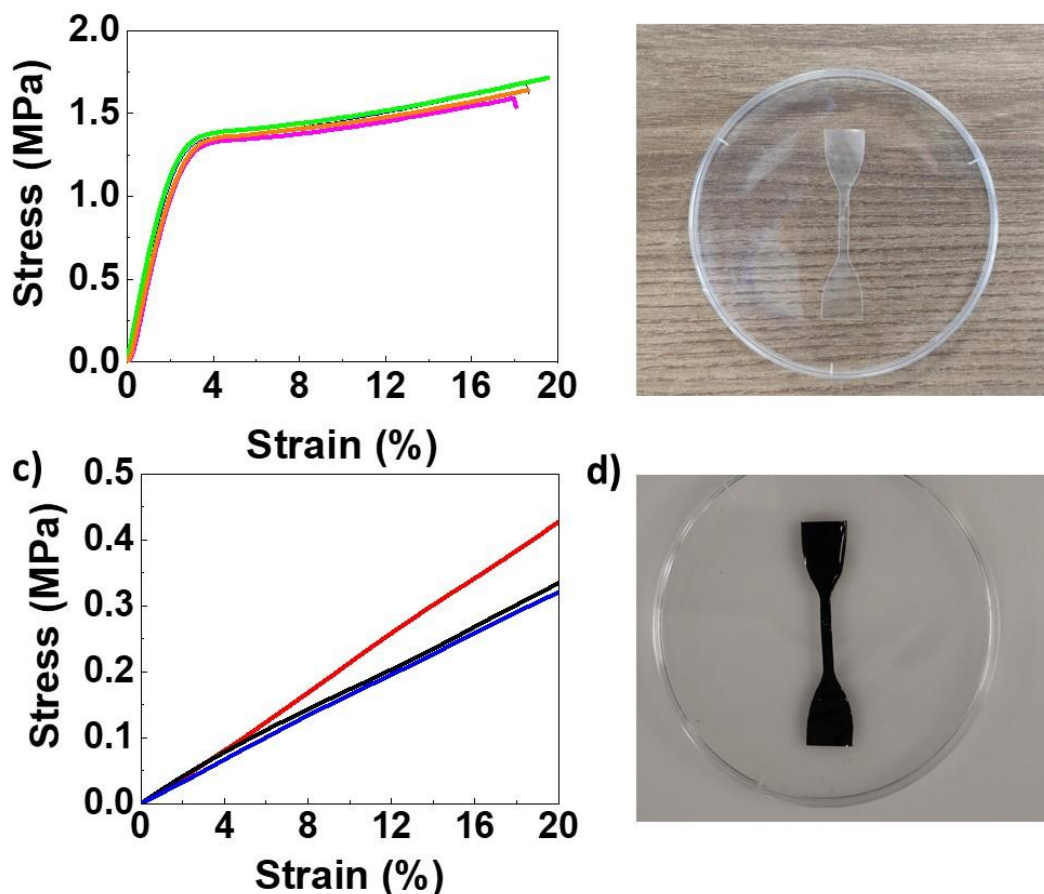


Figure S16. a) Stress/strain test of a CMC sample. b) Picture of the tested CMC sample. c) Stress/strain test of the PDMS/AgNPs sample (240 minutes of synthesis). Picture of the PDMS/AgNPs sample.

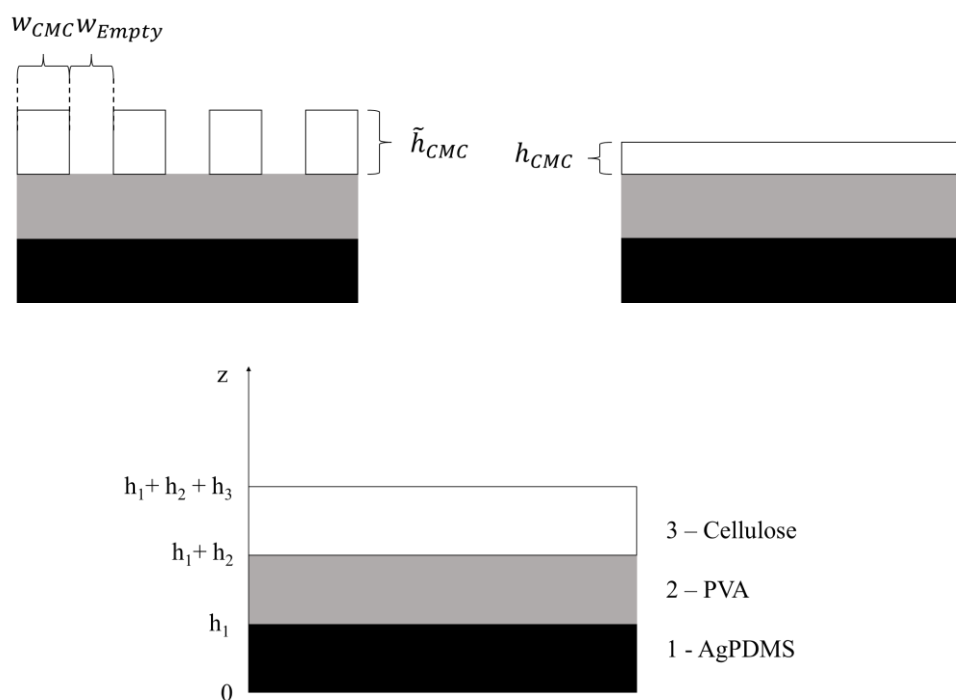


Figure S17. Sketch of the trilayer composite and its geometrical reference coordinates.

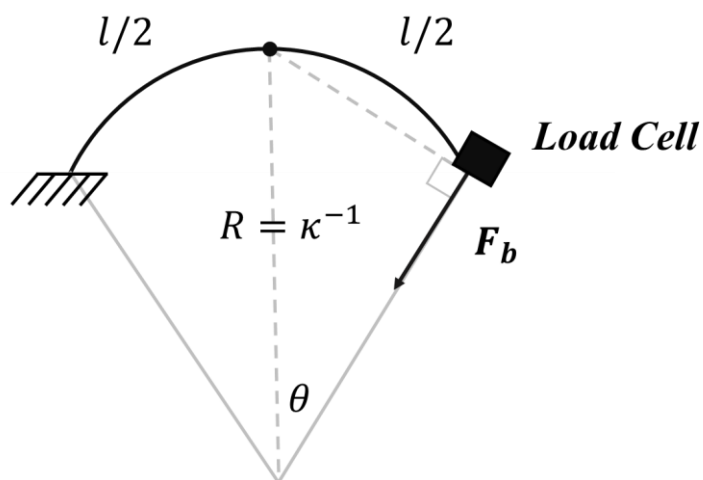


Figure S18. Sketch of the experimental setup for force measurement.

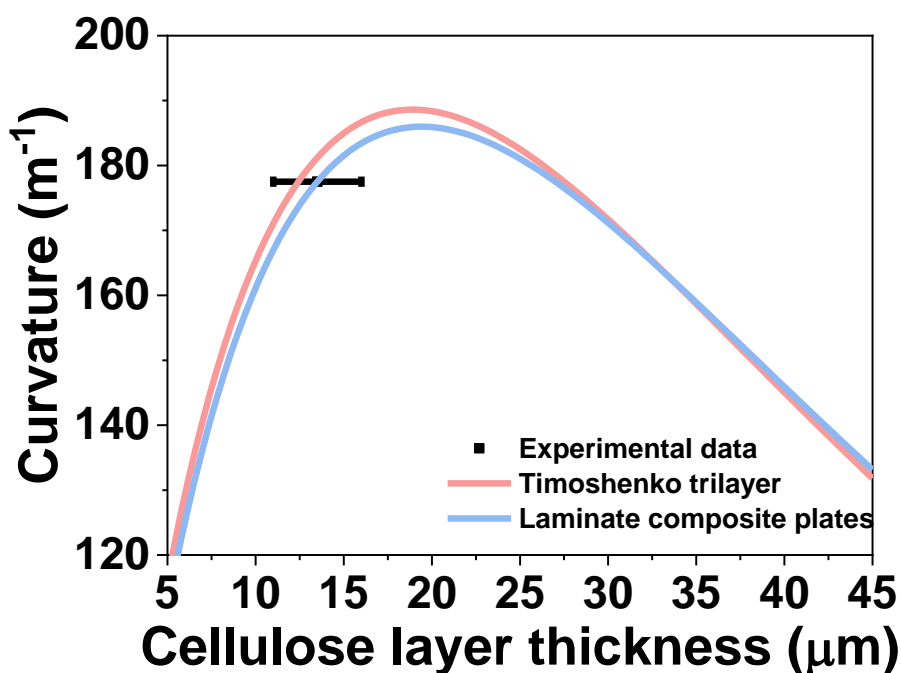


Figure S19. Prediction of the curvature for %RH=50%, using both the Timoshenko trilayer and the laminate composite plates models. Both models substantially provided the same trend, which was used in order to define DIW conditions, namely to achieve a high curvature while also avoiding coalescence of the CMC tracks. Based on the carried out experiments, the curvature of the fabricated actuator was in agreement (within a 95% confidence interval) with model predictions.

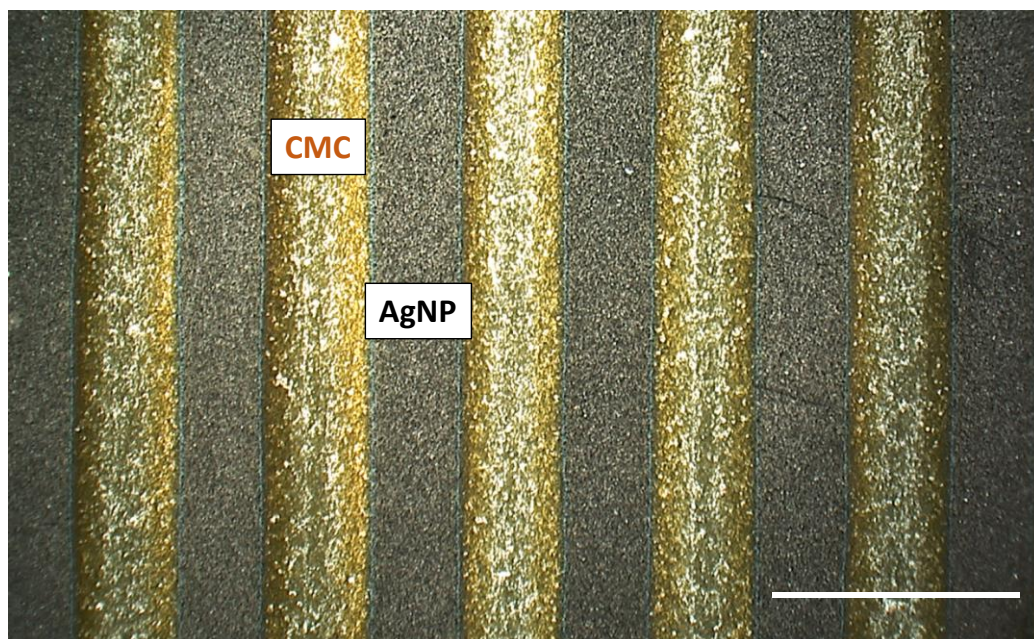


Figure S20. Optical microscope image of the top-view BL/PPTL/HL actuator surface. The black surface shows the BL/PPTL layer with a PDMS surface decorated with plasmonic AgNPs. The yellow/white tracks show the printed HL made of CMC. Scalebar is 2 mm.

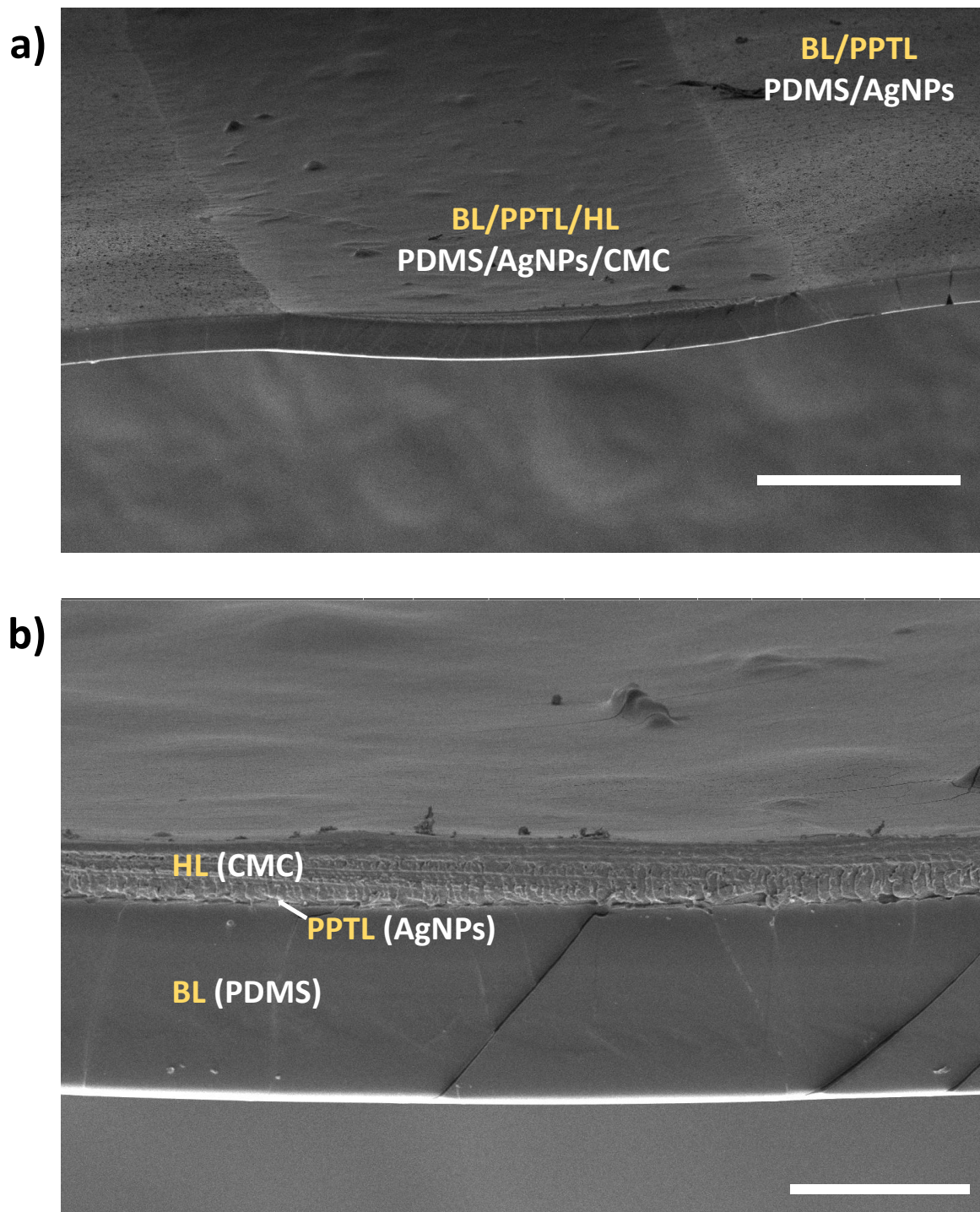


Figure S21. a) SEM image of a BL/PPTL/HL actuator section showing the PDMS/AgNPs and PDMS/AgNPs/CMC layers. Scalebar is 300 μm . b) Zoom of (a). Scalebar is 50 μm .

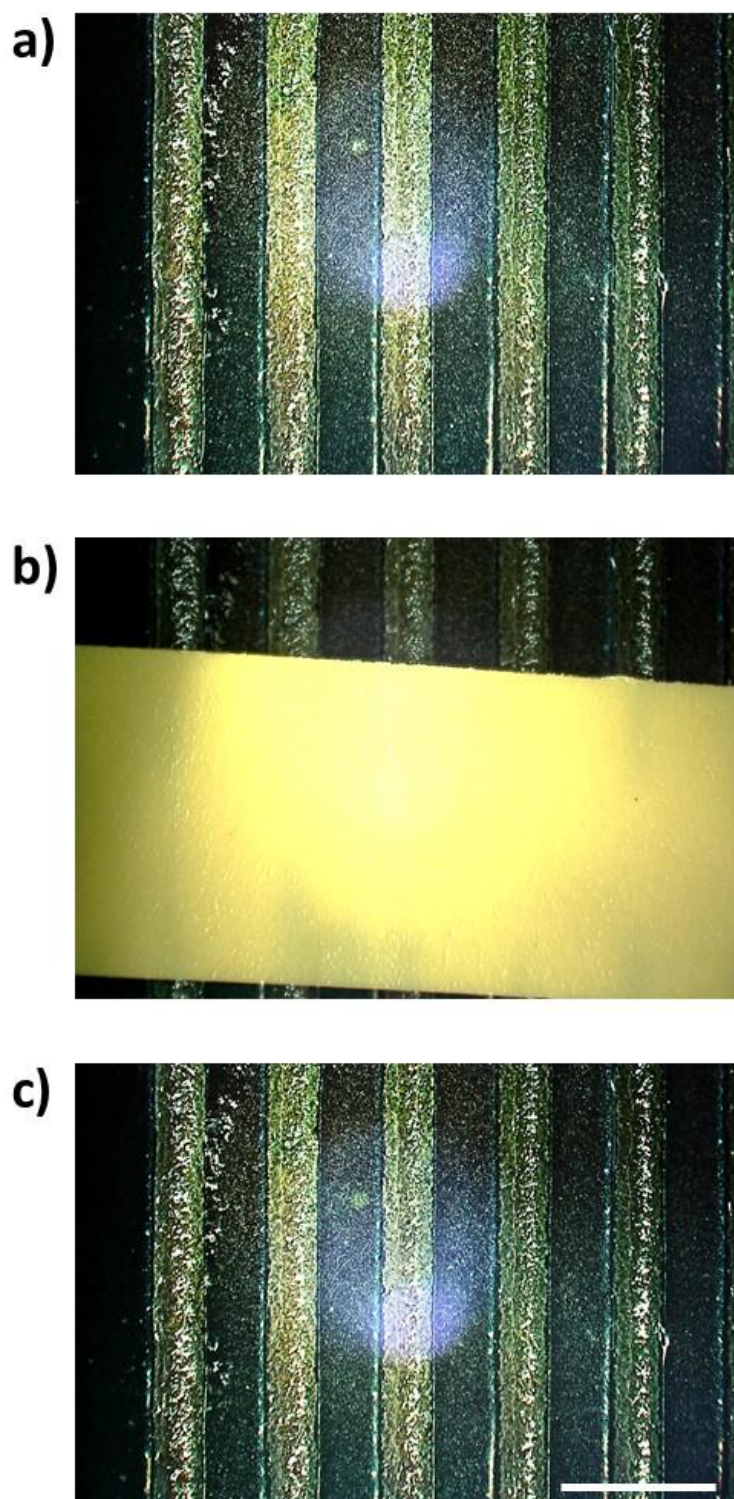


Figure S22. Optical microscope image of the top-view BL/PPTL/HL actuator surface before(a), during (b) and after (c) the tape test. Scalebar is 2 mm.

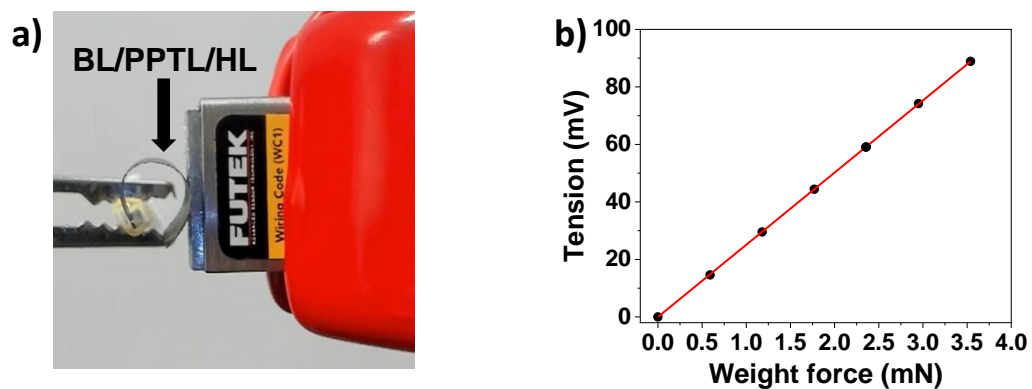


Figure S23. a) Loadcell setup for the PDMS/AgNPs/CMC actuator force measurement under humidity or sunlight stimulation. b) Calibration of the loadcell.

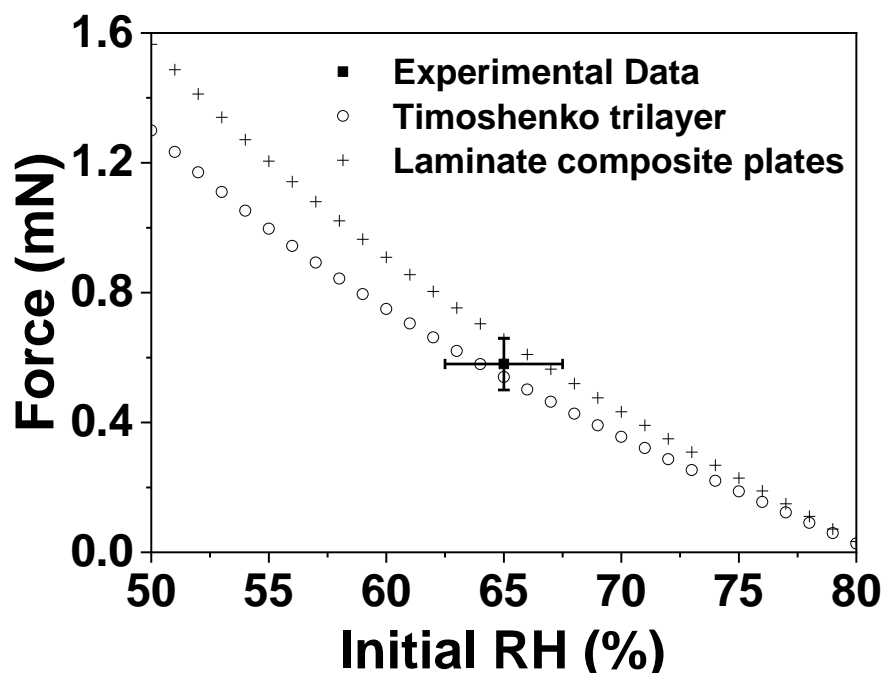


Figure S24. Prediction of the maximum force considering a variable RH initial condition and RH=80% as the final humidity value. Timoshenko and Laminate composite plates model predict the experimental results within a confidence interval of 95%.

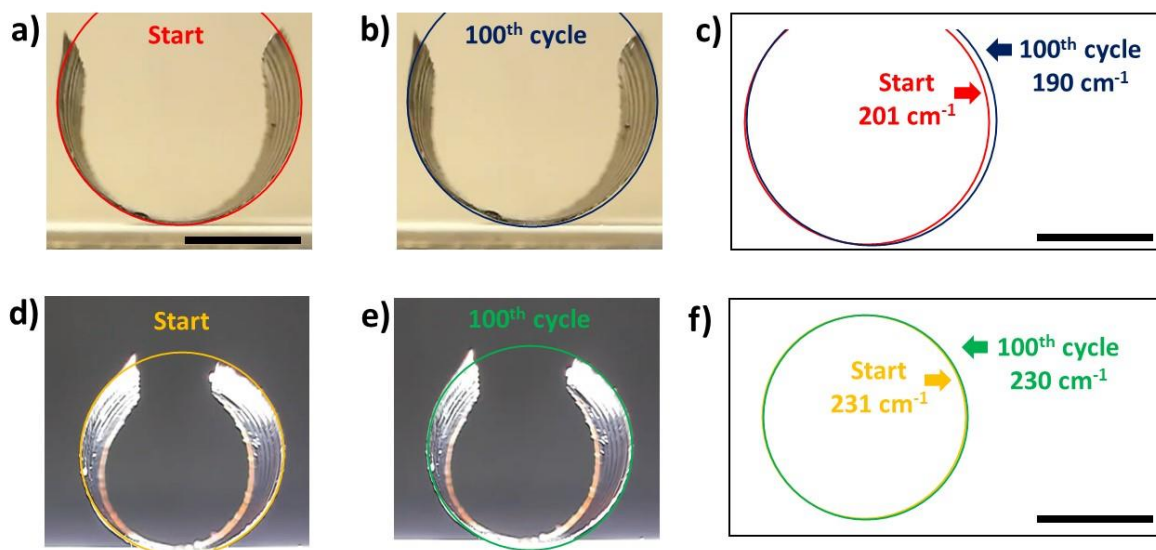


Figure S25. Bending performance retention test over cyclic irradiations: curvatures after 100 cycles with intermitting solar irradiation (20s 1 Sun irradiation /40s no irradiation). a) Picture of the actuator and curvature before the irradiation cycles. b) Picture of the actuator and curvature after 100 irradiation cycles. c) Curvature comparison before and after 100 irradiation cycles. d) Picture of the actuator and curvature during the 1st irradiation cycle. e) Picture of the actuator and curvature during the 100th irradiation cycle. f) Curvature comparison between the 1st and 100th irradiation cycle. Scalebar is 5 mm for (a-f).

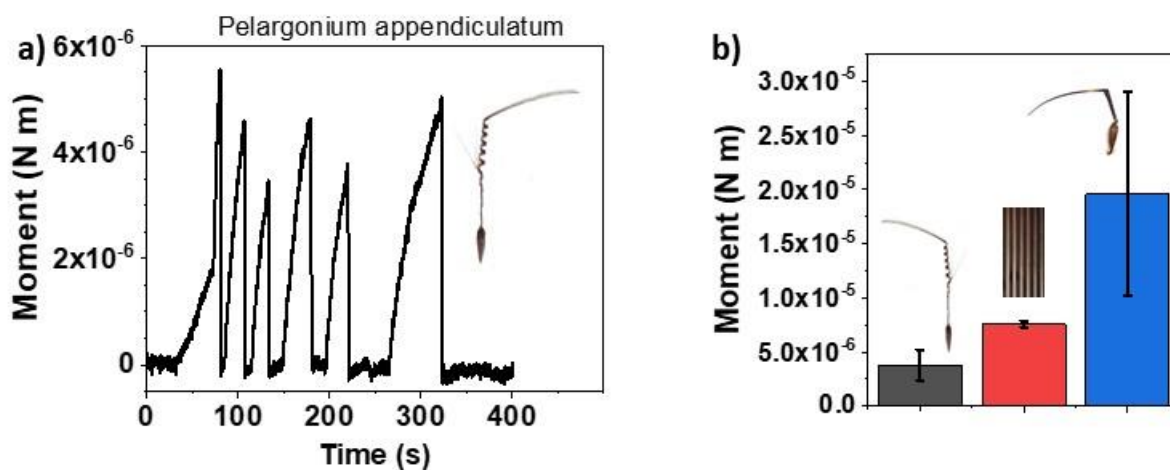


Figure S26. a) Moment (N m) of *Pelargonium appendiculatum* seed measured from fully wet to dry. b) Moment values of *Pelargonium appendiculatum* (grey bar) and *Erodium malacoides* (blue bar) compared to the BL/PPTL/HL actuator (red bar).

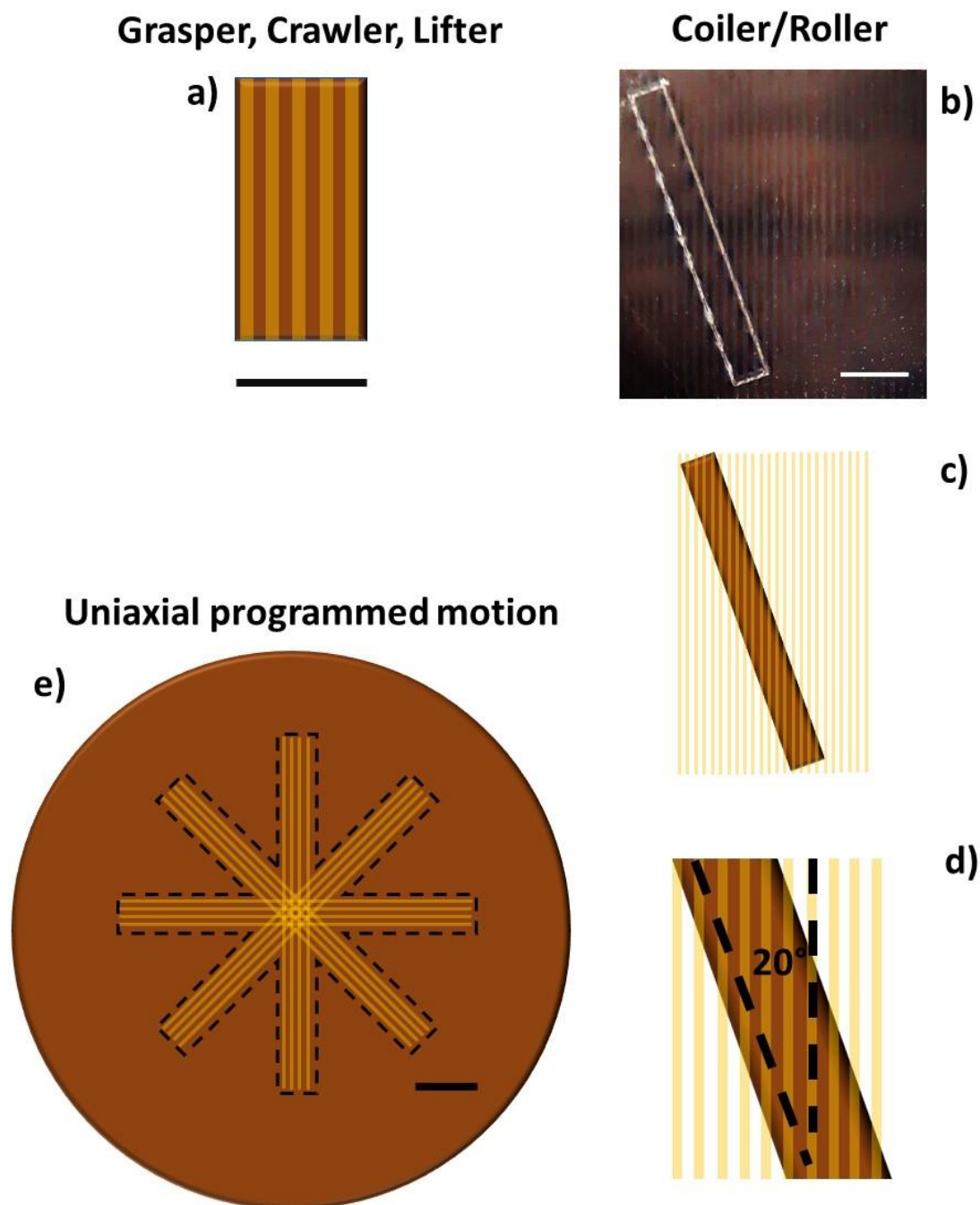
Section S5. Design of the actuators

Figure S27. a) Design of the grasper, crawler, lifter. Scalebar is 1 cm. In the case of the crawler 5 iron threads in front (bended at 110°) and 5 behind (straight) were glued on the short side of the rectangular actuator to create different friction forces between the two ends during the sunlight actuation. b-d) Design of the coiler/roller. b) Laser cut of the PDMS/AgNPs/CMC surface on a Petri dish. Scalebar is 1 cm. c) Sketch of the laser cut for the coiler/roller. d) Zoom from (c) showing the angle between the CMC tracks and the longitudinal axis of the actuator (i.e., 20°). e) Design of the light-responsive actuator devised for uniaxial programmed motion. Scalebar is 1 cm. In all the images the brown color depicts the PDMS/AgNPs layer (BL/PPTL), while the yellow lines represent the printed CMC tracks (HL).

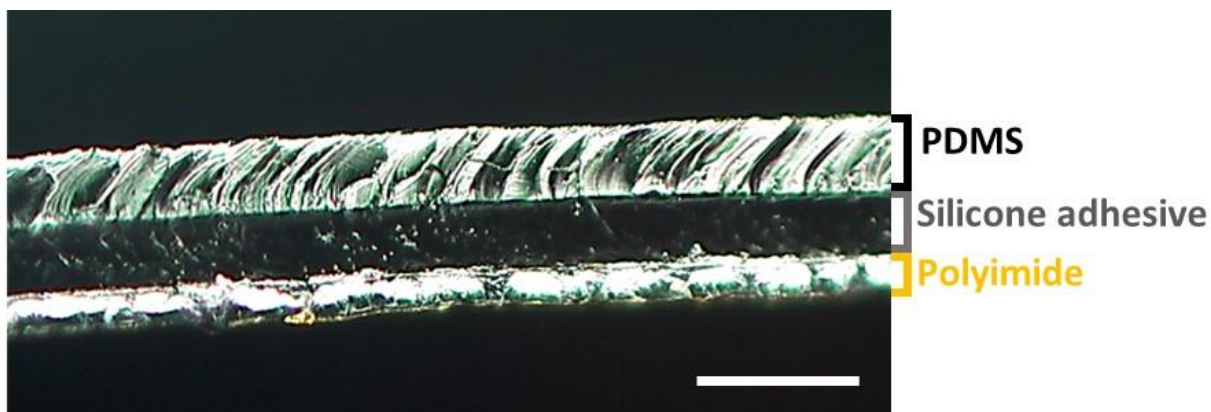


Figure S28. Optical image of a Polyimide/Silicone Adhesive/PDMS/AgNPs section employed for the development of the multilayered composite actuator. Scalebar is 100 μm . A PDMS/AgNPs/CMC rectangular actuator (2 cm \times 0.5 cm) was stuck on a Kapton tape (polyimide film) (tesa® 51408, Tesa, Italy) embedded with silicon adhesive, with a total thickness of 65 μm and with a tensile strength of 46 N/cm. A reversible actuation cycle is reported in Video S8 under irradiation of 1 Sun.

Reference

- [1] D. D. Han, Y. L. Zhang, H. B. Jiang, H. Xia, J. Feng, Q. D. Chen, H. L. Xu, H. B. Sun, *Adv. Mater.* **2015**, *27*, 332
- [2] J. Duan, F. Liu, Y. Kong, M. Hao, J. He, J. Wang, S. Wang, H. Liu, Y. Sang, *ACS Appl. Nano Mater.* **2020**, *3*, 1002.
- [3] Y. Hu, J. Liu, L. Chang, L. Yang, A. Xu, K. Qi, P. Lu, G. Wu, W. Chen, Y. Wu, *Adv. Funct. Mater.* **2017**, *27*, 1704388.
- [4] Y. Yang, Y. Liu, Y. Shen, *Adv. Funct. Mater.* **2020**, *30*, 1910172.
- [5] G. Cai, J. H. Ciou, Y. Liu, Y. Jiang, P. S. Lee, *Sci. Adv.* **2019**, *5*, 1
- [6] S. Zavaahir, P. Sobolciak, I. Krupa, D. S. Han, J. Tkac, P. Kasak, *Nanomaterials* **2020**, *10*, 1.
- [7] Y. Hu, L. Yang, Q. Yan, Q. Ji, L. Chang, C. Zhang, J. Yan, R. Wang, L. Zhang, G. Wu, J. Sun, B. Zi, W. Chen, Y. Wu, *ACS Nano* **2021**, *15*, 5294.
- [8] Y. Li, J. Wang, L. Huang, L. Chen, H. Gao, Y. Ni, Q. Zheng, *ACS Sustain. Chem. Eng.* **2022**, *10*, 6414-6425.
- [9] H. Zhao, X. Qi, Y. Ma, X. Sun, X. Liu, X. Zhang, M. Tian, L. Qu, *Nano Lett.* **2021**, *21*, 8126.
- [10] Z. Zhu, E. Senses, P. Akcora, S. A. Sukhishvili, *ACS Nano* **2012**, *6*, 3152
- [11] Q. Shi, H. Xia, P. Li, Y. Wang, L. Wang, S. Li, G. Wang, *Adv. Opt. Mat.* **2017**, 1700442, 1.
- [12] A. Mourran, H. Zhang, R. Vinokur, M. Möller, *Adv. Mater.* **2017**, *29*, 1604825.
- [13] H. Qin, T. Zhang, N. Li, H.-P. Cong, S.-H. Yu, *Nat. Commun.* **2019**, *10*, 2202.
- [14] M. Kim, J. Choi, S. Y. Kim, *Mater. Today Chem.* **2022**, *26*, 101014.
- [15] X. Yang, Y. Chen, X. Zhang, P. Xue, P. Lv, Y. Yang, L. Wang, W. Feng, *Nano Today* **2022**, *43*, 101419.
- [16] X. Lu, H. Zhang, G. Fei, B. Yu, X. Tong, H. Xia, Y. Zhao, *Adv. Mat.* **2018**, 1706597, 1.
- [17] J. Chen, J. Feng, F. Yang, R. Aleisa, Q. Zhang, Y. Yin, *Angew. Chemie Int. Ed.* **2019**, *58*, 9275.
- [18] F. Meder, G. A. Naselli, A. Sadeghi, B. Mazzolai, *Adv. Mater.* **2019**, *31*, 1905671.
- [19] Y. Wang, E. Sachyani Keneth, A. Kamyshny, G. Scalet, F. Auricchio, S. Magdassi, *Adv. Mater. Technol.* **2022**, *7*, 2101058.
- [20] T. Trantidou, Y. Elani, E. Parsons, O. Ces, *Microsystems Nanoeng.* **2017**, *3*, 16091.
- [21] C. A. Schneider, W. S. Rasband, K. W. Eliceiri, *Nat Meth* **2012**, *9*, 671.
- [22] T. Hamann, E. Smets, F. Lens, *Taxon* **2011**, *60*, 841.
- [23] K. Jiang, D. A. Smith, A. Pinchuk, *J. Phys. Chem. C* **2013**, *117*, 27073.
- [24] K. Yamaura, M. Tada, T. Tanigami, S. Matsuzawa, *J. Appl. Polym. Sci.* **1986**, *31*, 493.
- [25] J.-H. Lee, S.-S. Lee, J.-D. Chang, M. S. Thompson, D.-J. Kang, S. Park, S. Park, *Sci. World J.* **2013**, *2013*, 930798.
- [26] S. Khoshtinat, V. Carvelli, C. Marano, *Cellulose* **2022**, *29*, 2175.
- [27] S. Shrestha, J. A. Diaz, S. Ghanbari, J. P. Youngblood, *Biomacromolecules* **2017**, *18*, 1482.
- [28] B. Shapiro, E. Smela, *J. Intell. Mater. Syst. Struct.* **2006**, *18*, 181.
- [29] S. Armon, E. Efrati, R. Kupferman, E. Sharon, *Science (80-.)*. **2011**, *333*, 1726.